Effects of glass fiber properties and polymer molecular mass on the mechanical and tribological properties of a polyamide-66-based composite in contact with carbon steel under grease lubrication

Takeshi Kunishima, Yasuharu Nagai, Setsuo Nagai, Takanori Kurokawa, Gaëtan Bouvard, Jean-Christophe Abry, Vincent Fridrici, Philippe Kapsa

Effects of glass fiber properties and polymer molecular mass on the mechanical and tribological properties of a polyamide-66-based composite in contact with carbon steel under grease lubrication

Takeshi Kunishima[a, b], Yasuharu Nagai[a], Setsuo Nagai[a], Takanori Kurokawa[a], Gaëtan Bouvard[b], Jean-Christophe Abry[b], Vincent Fridrici[b], Philippe Kapsa[b]

[a] JTEKT CORPORATION, 333 Toichi-cho, Kashihara, Nara 634-8555, Japan

[b] Laboratoire de Tribologie et Dynamique des Systèmes, UMR CNRS 5513, Ecole Centrale de Lyon, Université de Lyon-36 avenue Guy de Collongue F-69134 Ecully cedex, France

Corresponding author: Takeshi Kunishima, E-mail: takeshi_kunishima@jtekt.co.jp

Keywords: Polyamide, Glass fibers, Wear, Grease, Composite, Molecular mass, Friction

ABSTRACT

Polyamide 66 is widely used for sliding parts that are in contact with steel under grease lubrication, including worm gears or bearing retainers. To meet the requirements for downsizing these parts and for their use under severe conditions, reinforcement fibers, such as glass fibers, are added to polyamide 66 to increase its strength and stiffness. However, the use of glass-fiber-reinforced polyamide 66 composites in sliding parts leads to wear and creep of the composites due to peeling of the fibers and scratching of polyamide 66 during sliding. Additionally, the aggressive effects of the hard fibers on the steel counterpart should be considered. In this study, the effects of the composition of glass-fiber-reinforced polyamide 66 on its tribological properties were investigated to aid in the development of a composite with optimal tribological properties. The results indicate that the use of higher-molecular-mass polyamide 66, smaller-diameter glass fibers, and a suitable glass fiber treatment agent to improve the interfacial adhesion of the fibers to polyamide 66 can enhance the wear and creep resistance of the composite and decrease the aggressive effect of the glass fibers on the steel counterpart, which occurs via two-body abrasive wear.

1. Introduction

Polyamide 66 (PA66) is a well-known engineering plastic with interesting properties including heat resistance, high strength, good toughness, and high wear resistance [1-4]. PA66 is often employed in sliding parts, including various types of gears [5-8], bearing retainers [9,10], and rollers [11] for automobiles or industrial machines. In particular, plastic worm gears are used as worm reducers in automobile electric power steering systems under grease lubrication to reduce friction and heat generation during sliding [12-14]. Downsizing or decreasing the weight of these plastic automotive components would allow improved fuel efficiency, and the ability to use plastic sliding parts under more severe conditions could widen their applications. Therefore, improvements in the mechanical properties of these plastic materials are required. To improve the mechanical properties and wear resistance of PA66, reinforcement fibers, such as glass fibers (GFs) or carbon fibers (CFs) are generally added [15-18]. In practical applications, both the wear and creep resistance of a composite part and the wear resistance of its steel counterpart must be considered, as wear or creep of either

material can lead to severe part deformation, insufficient part durability, and increased friction between the parts. In the case of worm gears, the machining and heat treatments (quenching and tempering) applied to the teeth of the steel worm shafts can affect the product performance and manufacturing costs. For example, heat treatment of a steel worm shaft before forming the teeth makes tooth formation much more difficult. However, heat treatment after tooth formation reduces the dimensional accuracy of the shaft due to the distortion caused by the treatment, reduces the meshing accuracy of the gears, and has an undesirable effect on product performance [19]. In a previous study, we investigated the tribological properties of a GF-reinforced PA66 composite in contact with carbon steel under high-contact-pressure, grease-lubricated sliding conditions. Sliding induces characteristic damage to the surface of the composite (peeling of the fibers and scratching of the PA66) and degradation of its mechanical properties, which in turn leads to an increase in the friction and creep of the composite. In addition, the GFs have an aggressive effect on the steel counterpart via a two-body abrasive wear mode. Furthermore, the effects of the hardness of the steel counterpart on the tribological properties of the system were investigated, and the use of a relatively harder steel counterpart was found to decrease the wear of the steel, but increase the wear and creep of the composite. These results indicated that the properties of the steel counterpart affect the wear resistance of both the composite and the steel counterpart itself [19]. In another paper from the same authors [20], the temperature dependence of the tribological properties of the GF-reinforced PA66 in contact with carbon steel was studied. The mechanical properties of the PA66 composite surface and the tribofilm formation related to the additives of grease at different temperatures well explained the temperature dependence of the tribological properties. However, the previous studies were conducted using a single type of GF-reinforced PA66 composite, and the effects of the composition of the composite were not investigated. Therefore, the development of guidelines for the formulation of GF-reinforced PA66 composites with good wear and creep resistance and low aggressive effects on their steel counterpart is necessary.

The interfacial shear strength between the PA66 and the GFs, the diameter of the GFs, and the molecular mass of the PA66 are the most important parameters in terms of the properties of the GF-reinforced PA66 composite, as these parameters directly influence its mechanical properties. The surface of the fibers is often treated with a coupling agent or compatibilizer to increase the interfacial shear strength between the matrix resin and the fibers [21]. The reaction between the reactive functional groups on the surface agent and the polymer ensures good adhesion between the fibers and polymer. Aminosilane coupling agents are a representative class of surface agents used to ensure adhesion between GFs and several types of polymers [21, 22]. Polyurethane resins are also used as surface treatment agents for reinforcement fibers [23, 24]. The effects of the adhesion between the fibers and the matrix resin of composites on their tribological properties have been studied [25-28]. Karsli et al. [25] found that the addition of 2 wt% 1,4-phenylene-bis-oxazoline as a coupling agent increases the interfacial adhesion between GFs and PA66 and improves the adhesive wear resistance of a GF-reinforced PA66 composite in contact with a ceramic ball under dry conditions. Karsli et al. [26] also reported that thermal aging of GF- or CF-reinforced polyether ether ketone composites at 360 °C improves the interfacial adhesion between the fiber–matrix surface as measured by dynamic mechanical analysis (DMA) due to the formation of a transcrystalline phase between the fibers and the matrix resin during aging. However, few studies have focused on the effects of the interfacial strength between fibers and polymer matrices on the wear resistance of

composites under grease lubrication. In particular, the effects of the two-body wear resistance of the steel counterpart caused by the presence of GFs have not been investigated. Therefore, the quantitative discussion on the effect of the interfacial shear strength of GF and PA66 on the tribological properties under grease lubrication should be conducted.

The molecular mass of PA66 is also known to affect the tribological properties of polymers or composites with a PA66 matrix [29-31]. Shin et al. [29] reported that the wear of unreinforced or GF-reinforced PA66 in contact with carbon steel under dry conditions is dominated by the adhesion of PA66 to the counter surface. The wear rate and friction coefficient of the unreinforced PA66 and GF-reinforced PA66 increase with the increase in the molecular mass of PA66 as a result of its increased adhesion to the counter surface at high temperatures due to the low tensile strength of high-molecular-mass PA66. The authors also reported that the addition of GFs decreases the wear and friction coefficients due to the reduced adhesion of PA66 to the steel counterpart. Kunishima et al. [30] reported the tribological properties of GF- and aramid fiber (AF)-reinforced PA66 composites containing the additive carbodiimide in contact with steel in the presence of barium complex grease. Unlike Shin, they found that the toughness and wear-resistance of the PA66 composite are improved by increasing the molecular mass of PA66 due to the reactive extrusion process between PA66 and the poly-carbodiimide compounds. Therefore, in their study, the effect of increasing the molecular mass of PA66 was different than in the study of Shin et al. However, neither the mechanism by which the higher molecular mass improved the tribological properties of the composite nor the mechanism of the wear of the steel counterpart were discussed in this study. Therefore, a detailed investigation of the tribological behavior of the composite and steel under grease-lubricated conditions is necessary.

The diameter of the GFs also affects the mechanical properties of PA/GF composites. Ramsteiner et al. [32] investigated the effect of the GF diameter on the static mechanical properties of GF-reinforced polyamide; in this study, the GFs were treated using the same surface agent and exhibited the same interfacial shear strength with the polyamide; only their diameter was varied. The diameter of the fibers (10–24 μm) does not have a strong influence on the Young's modulus of the composite, which is only affected by the amount of fibers. In contrast, the fracture strength of the composite was found to be significantly influenced by the diameter of the GFs. The diameter of the fibers influences the stress concentration of the fibers, with increasing fiber diameter decreasing the strength of the composite. Ozawa et al. [33] reported that the static tensile strength and impact strength of GF-reinforced PA66 increases with decreasing GF diameter under the same fiber orientation conditions. They found that the strength value predicted using a modified Kelly–Tyson model correlates well with the measured value when the strain rate of the test is taken into account. They showed that the load that can be borne by the entire interface when the strain rate of the test is taken into account increases with decreasing GF diameter due to the resulting increase in the interfacial area between the GFs and PA66, and that decreasing the critical fiber length can allow the fibers to bear higher loads. Murakami et al. [34] reported that the static strength, impact strength, and fatigue properties of GF-reinforced PA66 with small-diameter GFs are superior to those of normal-diameter-GF composites. The small-diameter GFs mitigate the stress concentration, which improved the durability of a composite worm gear for an electric power steering system. However, very few studies have reported the effects of GF diameter on the tribological properties of GF-reinforced composites

under either dry or grease-lubricated conditions.

To address the gaps in knowledge highlighted above, the present study focuses on the effects of the molecular mass of PA66, the diameter of the GFs, and the interfacial strength of the GFs and PA66, which is determined by the GF surface treatment agent, on the tribological properties of GF-reinforced PA66 in contact with steel under grease lubrication. Composite specimens were designed specifically to clarify the effects of each of these material parameters separately, and the effects of these parameters on the wear or creep resistance of the composite, the wear resistance of the steel counterpart, and the friction coefficient were elucidated and explained in terms of the mechanical properties and the condition of the sliding surface.

2. Experimental

2.1 Experimental set-up and testing conditions

Traction tests were conducted according to the standard ISO527 to measure the tensile mechanical properties of each sample; Table 1 presents the test conditions. The Young's modulus of the sliding surface of the steel cylinder, and the Young's modulus and hardness of the GF-reinforced PA66 composite ring according to the standard JIS K 7218 (testing methods for sliding wear resistance of plastics) were measured via a micro-indentation process. Table 2 lists the measurement conditions. Sliding tests in which the composite ring was in contact with four steel cylinders under grease-lubricated conditions were conducted to evaluate the tribological properties of each composite sample. This is an original test method developed by us that allows a high contact pressure to be applied; the test was carried out in the same way as in our previous work [19, 20, 30]. A schematic of the test specimens and tribometer is shown in Fig. 1. The sliding tests were performed under grease-lubricated conditions using 0.85 g of grease for each test. The height and weight decrease of each specimen were measured. In this way, the creep and wear could be estimated separately, and the individual contributions of creep and wear could be discussed. The total height decrease (h_{total}, the difference in the height of a specimen before and after tests) is the sum of the wear and creep of the composite. The wear height loss (h_{wear}) can be estimated using the following equation:

$$h_{wear} = \frac{M_{wear}}{ds} \qquad (1)$$

where M_{wear} is the wear mass of the composite, d is the density of the composite (1.23 g/cm^3 in 15% GF reinforced PA66 composite), and s is the area of the sliding surface (approximately 200 mm^2). The creep height loss (h_{creep}) was calculated by subtracting h_{wear} from the total height decrease.

$$h_{creep} = h_{total} - h_{wear} \qquad (2)$$

In addition, the vertical displacement of the holder of the four steel cylinders was measured in situ during the tests. In these tests, a thermocouple measured the temperature of the steel cylinder holder. A friction torque sensor measured the friction torque, and the friction coefficient was calculated using the following equation:

$$\mu = \frac{T}{rN} \qquad (3)$$

where T is the friction torque, N is the normal load, and r is the mean radius of the ring (11.4 mm). The friction coefficient was recorded as the average for each 1 s interval. One cycle in this test corresponded to one rotation of the ring specimen. Table 3 lists the conditions of the sliding test. Optical microscope and scanning electron microscopy (SEM) images of the sliding surfaces of the ring specimens were acquired after the sliding tests. The wear scars on the cylinders were observed using interferometry and used to estimate the wear volume.

Table 1 Test conditions for the tensile tests.

Tensile test specimen	Dimensions	150 × 10 × 4 mm
Test conditions	Tensile speed	5 mm/s
	Temperature	25° C
Measured properties		- Tensile strength - Young's modulus -Tensile elongation at breakage -Tensile breakage energy

Table 2 Micro indentation test conditions.

Measured sample	Steel cylinder	Composite ring
Type of indenter	Vickers	Vickers
Maximum normal load	300 mN	1,500 mN
Indentation test procedure	Load: 0→300 mN for 10 s Creep: 300 mN for 5 s Unload: 300 mN⇒40 mN for 4 s	Load: 0→1,500 mN for 10 s Creep: 1,500 mN for 5 s Unload: 1,500 mN⇒40 mN for 4 s

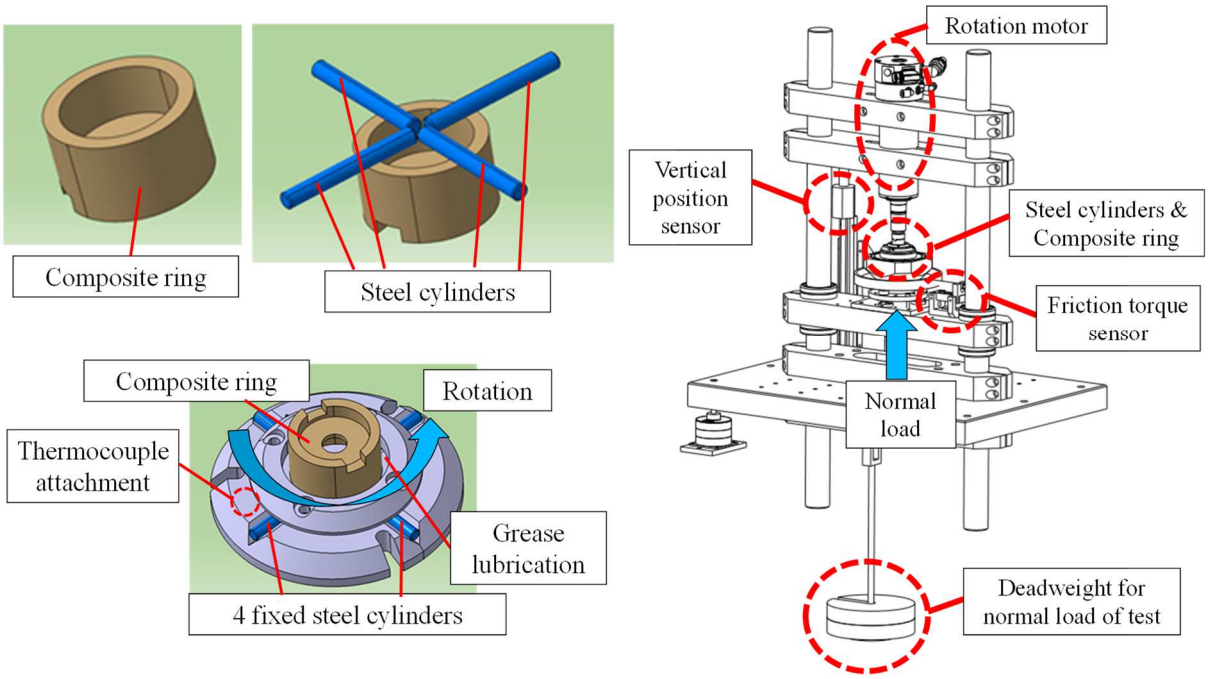

Fig. 1 Schematic view of the test specimens and sliding test setup.

Table 3 Test conditions for the sliding tests.

Steel cylinders (×4)	Diameter	3.5 mm
	Length	30 mm
Composite ring specimen (JIS K 7218)	Outer diameter	25.6 mm
	Inner diameter	20 mm
	Height	12 mm
Test conditions	Rotation speed	790 rpm
	Mean sliding speed	1 m/s (Mean radius of the contact area: 11.4 mm)
	Normal load	350 N
	Total test duration	9.3–200 min: intermittent process (10 s sliding and 1 s stopping)
	Total sliding cycles	650–140,452
	Ambient temperature	25 °C
	Lubrication	Grease

2.2 Steel cylinders

The steel cylinders were composed of S45C steel, which contains 0.45% carbon, and met the standard JIS G 4051. Centerless grinding of the cylinders was conducted to achieve a surface roughness (Sa) of 0.18 μm. The Young's modulus of S45C and hardness of the steel cylinders measured through micro-indentation are listed in Table 4.

Table 4 Mechanical properties of the steel cylinders. Values of the hardness are the average values for 5 measurements.

Young's modulus	Hardness measured using micro-indentation
205 GPa [35-37]	4.7 +/- 0.1 GPa

2.3 Composite material

To prepare the GF-reinforced composite test specimens, unreinforced PA66 was prepared for extrusion as described in our previous work [19, 20]. The effects of the molecular mass of PA66, the GF surface treatment agent, and the GF diameter were investigated individually. Table 5 lists the compositions of the tested composites and the Hertzian contact pressures in the sliding tests with a normal load of 350 N. To investigate the effects of molecular mass, unreinforced PA66 pellets with three different molecular mass values were used as the raw PA66 material. E-glass fiber strands with different diameters (6.5–19 μm) were bundled and treated with a surface agent. Generally, the diameter of GFs added to engineering plastics (including PA66) is mainly in the range of 9-15 μm [16, 18, 38, 39, 43]. In the present work, GFs with much smaller (6.5 μm) and larger diameter (19 μm) were used additionally to evaluate the effect in a wider range of GF diameter. The GF strands were then cut to a length of 3 mm. In this study, commercially available chopped GF strands were treated with one of two different GF surface treatment agents (type A and type B) to evaluate the effect of the interfacial shear strength between the GFs and PA66 on the tribological properties of the composite. GF surface treatment agent type A was specifically developed for the adhesion of PA66 and GFs, while type B was developed for the adhesion of another polymer and GFs. Extrusion of PA66 and the chopped GF strands was carried out using a twin-screw extruder (TEM-26SX, Toshiba Machine Co., Ltd.). PA66 was fed from the root of the extruder barrel, and the GFs were fed from the middle of the extruder barrel. The tensile test specimens and sliding test specimens described in Section **2.1** were prepared through injection molding of the extruded pellets with an injection molding machine (ROBOSHOT S-2000i 100B, Fanuc Corporation). Furthermore, sample 4 was subjected to solid-state post-condensation to increase the molecular mass of the test specimen; the post-condensation was conducted at 220 °C for 10 h and under vacuum conditions to avoid the oxidation of PA66. The viscosity number (VN), which serves as a measure of the molecular mass of PA66, was measured using the relative viscosity method according to the standard ISO307. The ring specimens were cut by 3 mm in the height direction using a lathe. Additionally, the sliding surface of the ring was polished using #600 emery paper to simulate the exposure of the GF on the sliding surface of actual worm gear teeth due to the hob-cutting method

used to prepare such gears.

Table 5 Composition and properties of test specimens.

No.	VN of raw PA66	GF content	GF diameter	GF surface treatment agent	Solid-state post-condensation	VN of the specimen	Tensile Young's modulus	Hertzian maximum contact pressure
1	235 ml/g	15 wt%	6.5 µm	Type A	-	193 ml/g	6.0 +/- 0.4 GPa	191 MPa
2	235 ml/g	15 wt%	6.5 µm	Type B	-	-	6.0 +/- 0.4 GPa	191 MPa
3	150 ml/g	15 wt%	6.5 µm	Type A	-	145 ml/g	5.9 +/- 0.3 GPa	189 MPa
4	302 ml/g	15 wt%	6.5 µm	Type A	-	235 ml/g	5.4 +/- 0.6 GPa	181 MPa
5	302 ml/g	15 wt%	6.5 µm	Type A	220 °C × 10 h	356 ml/g	6.0 +/- 0.1 GPa	191 MPa
6	235 ml/g	15 wt%	9.5 µm	Type A	-	-	5.9 +/- 0.4 GPa	189 MPa
7	235 ml/g	15 wt%	11 µm	Type A	-	-	6.3 +/- 0.4 GPa	-
8	235 ml/g	15 wt%	13 µm	Type A	-	-	6.5 +/- 0.9 GPa	198 MPa
9	235 ml/g	15 wt%	15 µm	Type A	-	-	6.2 +/- 0.6 GPa	-
10	235 ml/g	15 wt%	19 µm	Type A	-	-	5.8 +/- 0.1 GPa	188 MPa

2.4 Grease

PAO8 (Polyalphaolefin 8) was used as the base oil of the grease in this study. The thickener consisted of urea-type compounds. Zinc carboxylate was added to decrease friction. A sulfur-type anti-oxidation agent was also added to prevent oxidation in high-temperature environments.

2.5 Image analysis of the sliding surface of the GF-reinforced PA66 composite

In order to understand the aggressive effects of the GFs on the steel counterpart, the fiber orientation at the sliding surface of the composite ring was evaluated quantitatively using image analysis in the same way as in our previous work [19]. First, the sliding surface of the ring specimen was polished using #4000 emery paper, and three SEM images of the inner/center/outer positions were obtained at a magnification of ×300 in backscattered electron (BSE) mode, as shown in Fig. 2 (composite sample 1 is used as an example). Next, the PA66 and GF areas were separated by binarization using the software imageJ by Wayne Rasband (Fig. 3), and the total area of the GFs and total perimeter of the GFs (which is a measure of the total contact area between the GFs and PA66) were calculated. The circularity of each GF was calculated using the following equation:

$$C = \frac{4\pi S}{L^2} \qquad (4)$$

where C is the circularity of the GF particle, S is the surface area of the GF particle, and L is the perimeter of the GF particle. Circularity is an indicator of the orientation of the GF at the sliding surface. Circularity values close to 1 correspond to a circular shape, which in turn indicates that the GF is oriented perpendicular to the sliding surface. In contrast, lower circularity values correspond to elliptical or fibrous shapes, which indicate that the

GF is oriented parallel to the sliding direction.

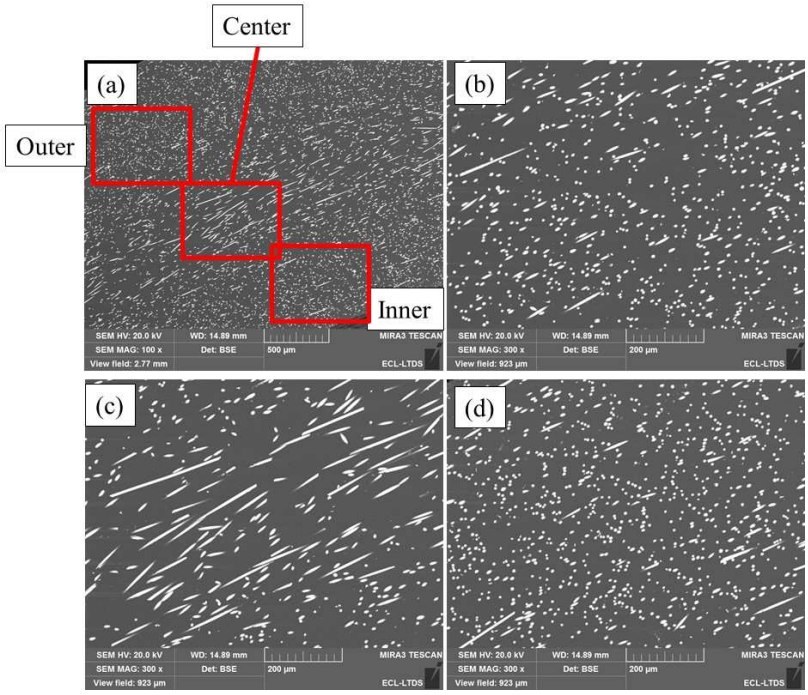

Fig. 2 SEM BSE images of the sliding surface of composite sample 1 at different locations: (a) Global view; (b) inner position; (c) center position; (d) outer position.

Fig. 3 Image analysis process: (a) Obtained SEM image; (b) binarized image; (c) image showing particle analysis.

3. Results and Discussion

3.1 Effects of the interfacial shear strength between the GFs and PA66 on the mechanical and tribological properties

First, the effect of the interfacial shear strength between GF and PA66 on the mechanical properties was studied, using the GF composites with fixed GF diameter (6.5 μm) and molecular mass of PA66 (VN: 145 ml/g) to investigate only the effect of the GF surface treatment agent. Table 6 compares the effect of the two different GF surface treatment agents (i.e., composite samples 1 and 2) on their tensile mechanical properties (tensile strength, Young's modulus, tensile elongation at break, and tensile breakage energy, along with the integral of

the stress–strain curve obtained in the tensile test, which serves as a measure of the toughness of composites). The tensile strength, tensile elongation at break, and tensile breakage energy of the composite in which the GFs were treated with the type A surface treatment agent were higher than those of the type B sample by 8.1%, 43.3%, and 78.7%, respectively. In contrast, no difference was observed among the Young's moduli of the composites. These results indicate that the choice of GF surface treatment agent only affected properties related to the breakage of the composite. This tendency is also reported in [40]. The Young's modulus was calculated from the initial slope of the stress–strain curve; thus, it was not affected by the GF surface treatment agent, but was instead determined exclusively by the GF content of the composite.

Table 6 Effects of the GF surface treatment agent on the mechanical properties of composites that differed only in the GF surface treatment agent used. The values are averages of five measurements, representing the standard deviation.

	Type A	Type B
Tensile strength	154.0 +/- 0.4 MPa	142 +/- 2.9 MPa
Young's modulus	6.0 +/- 0.4 GPa	6.0 +/- 0.4 GPa
Tensile elongation at break	5.1 +/- 0.1 %	3.5 +/- 0.2 %
Tensile breakage energy	10.9 +/- 0.2 J	6.1 +/- 0.6 J

Next, the effect on the tribological properties was investigated. Fig. 4 shows the evolution of the friction coefficient, temperature, and vertical displacement during the sliding tests of samples 1 and 2. Using the type B sample, which exhibited poorer mechanical properties, sudden increases in the friction coefficient were observed after 4,100/6,100 cycles, 14,200/21,000 cycles, and 48,700/61,600 cycles in the first and second repetitions of the sliding test, respectively. Little increase in the vertical displacement was observed after the first increase in the friction coefficient at 4,100/6,100 cycles; however, the displacement increased significantly following the friction coefficient increase at 14,200/21,000 cycles. The displacement then increased gradually until another large increase in the displacement was observed after the final friction coefficient increase at 48,700/61,600 cycles. In contrast, the friction coefficient and temperature of the type A sample were lower than those of the type B sample, particularly after 6,000 cycles, and no sudden increases in the friction coefficient or displacement were observed until 66,400 and 80,000 cycles in the first sliding test and 80,000 cycles in the second, respectively. Based on these results, the tribological properties of the composite in which the GFs were treated with type B were worse than those of the type A sample; this tendency was in agreement with the results of the tensile mechanical property tests.

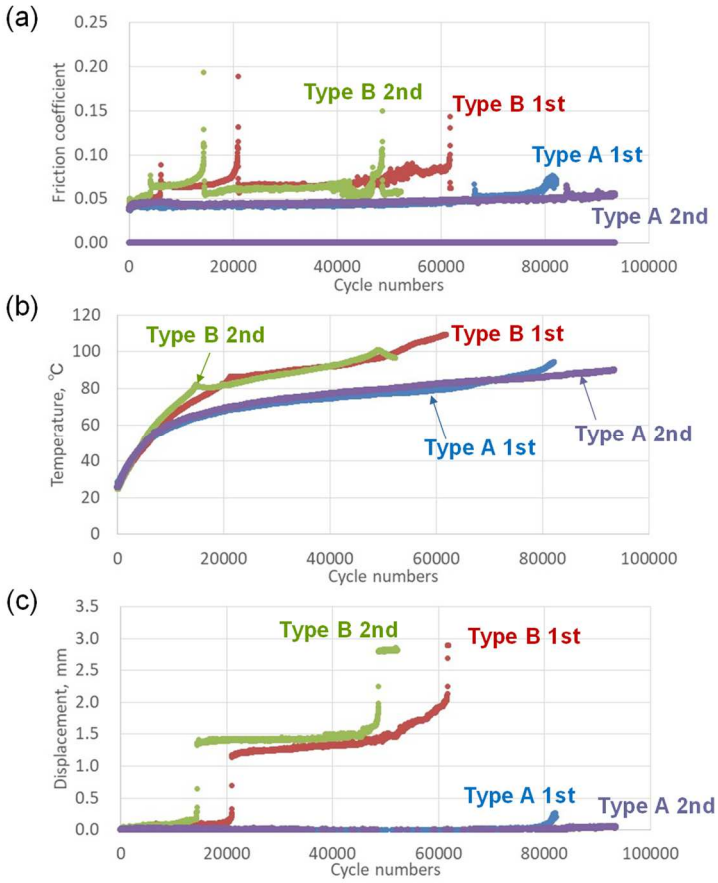

Fig. 4 Evolution of (a) the friction coefficient, (b) temperature, (c) and vertical displacement of composite samples that differed only in the GF surface treatment agent used.

To clarify the mechanism by which the different GF surface treatment agents induced different tribological properties, the sliding tests were intentionally stopped at 6,500 cycles (just before the first sudden increase in the friction coefficient of the type B sample) and at 22,300 cycles (between the first and second increases in the friction coefficient of the type B sample), and the sliding surfaces of the two samples were analyzed and compared. Fig. 5 presents the wear and creep height loss of the samples at 6,500 and 22,300 cycles. Little wear was observed for either of the samples at either of the measurement points; most of the height decrease was due to creep. These results confirmed that the significant increase in the displacement observed in Fig. 4 was mainly due to creep via plastic deformation. This increase in the vertical displacement which is considered to be the creep (plastic deformation which accompanies small weight loss due to wear) was also observed in the authors' previous study [19], and this creep was caused by the decrease in the surface mechanical properties related to the damage through cyclic loading of the sliding, such as the scratching of PA66 or peeled off of fibers. The creep height loss values for the type B sample were much greater than those of the type A sample at both cycle numbers, whereas the wear height loss values were relatively similar for both samples. Fig. 6 shows SEM images of the center position of both composite surfaces after 6,500 cycles and 22,300 cycles. At both measurement points, greater amounts of interfacial GF peeling, peeled GFs, and holes originating from GFs, which were also observed in the previous study [19], were observed for the type B composite than for the type A

composite. Additionally, particularly after 22,300 cycles, no severe GF breakage was observed on the type B composite; the GFs remained intact with long fiber length, but gaps between the GFs and PA66 were present due to poor adhesion of the fibers to the PA66. In contrast, the GFs used in the type A composite were shortened and damaged; however, good adhesion between the GFs and PA66 was maintained. These observations indicate that the interfacial adhesion of the GFs treated with type A to PA66 was stronger than that of those treated with type B, and that peeling of the type B GFs from the PA66 by the shear force during sliding occurred more readily than breakage of the GFs themselves due to the weak GF/PA66 adhesion. Therefore, the mechanical properties of the type B composite surface were easily degraded, leading to scratching of the PA66. Additionally, based on the wear and creep mechanisms of the composite in this tribosystem, which were elucidated in our previous study [19], we concluded that propagation of the scratches and creep-related height loss occurred earlier due to the low toughness of the type B composite.

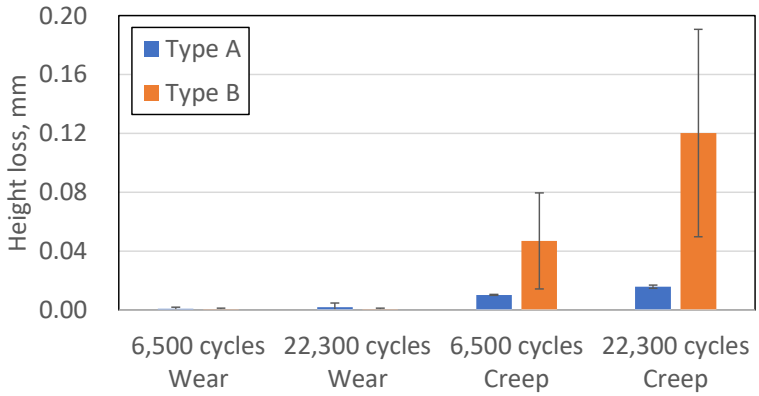

Fig. 5 Wear and creep height losses at different cycle numbers in composites that differed only in the GF surface treatment agents used.

(a)

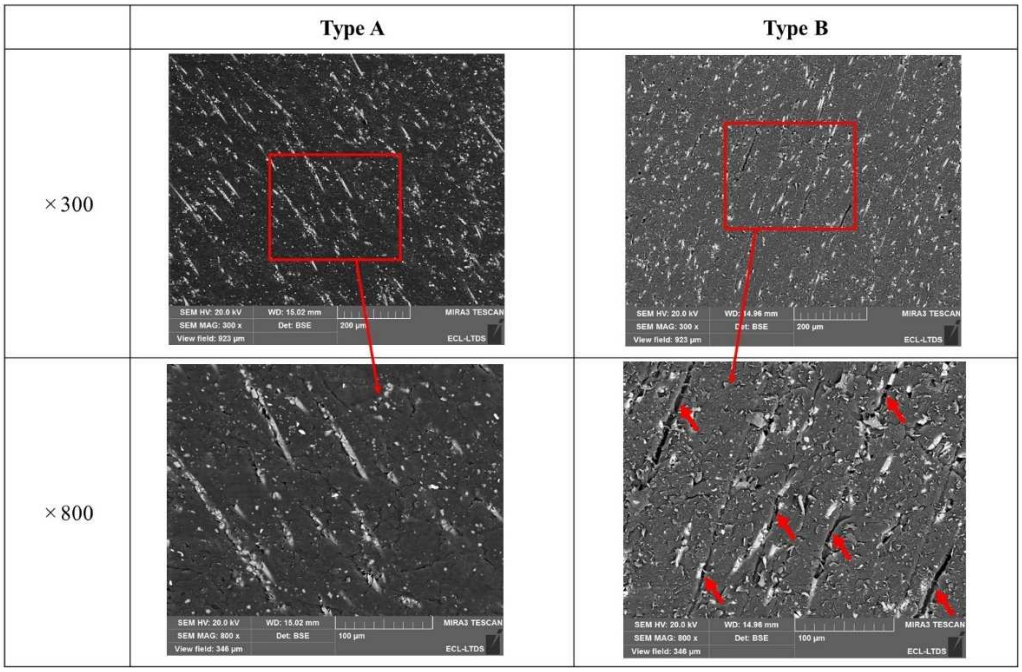

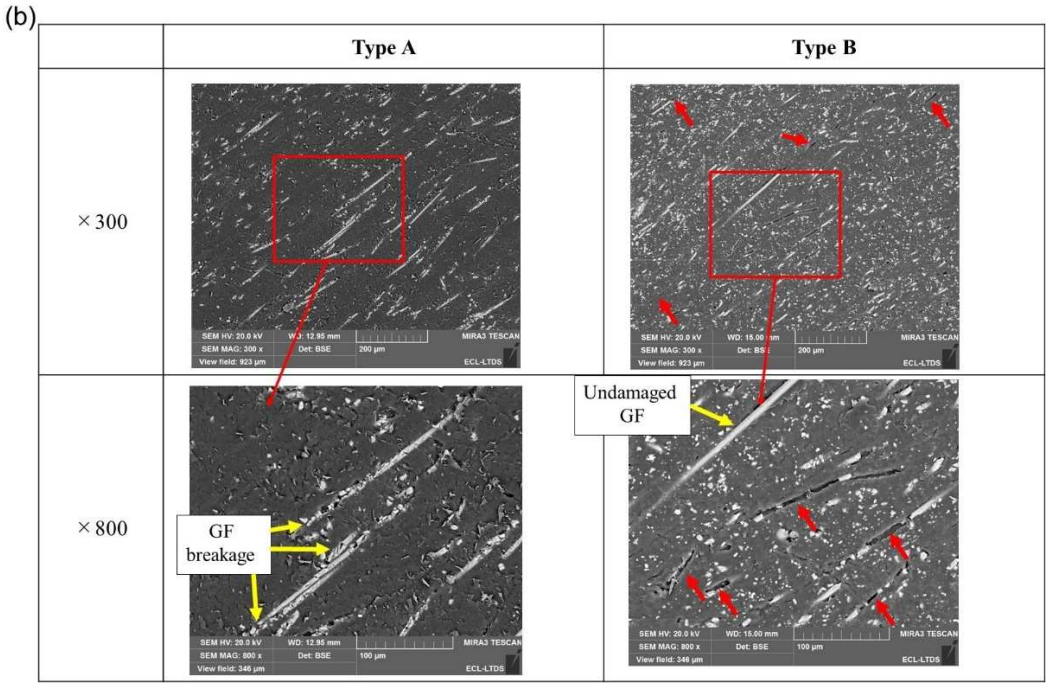

Fig. 6 SEM images of the sliding surfaces of the composites fabricated using different surface treatment agents (a) after 6,500 cycles and (b) after 22,300 cycles. Red arrows indicate holes originating from the detachment of GFs from the composite.

The effect of the adhesion between the PA66 and GFs on the wear of the steel counterparts was also investigated. Fig. 7 presents the wear volumes of the steel counterparts (total wear of the four steel cylinders, measured through interferometry) after the sliding tests with composites fabricated using different GF surface treatment agents, and Fig. 8 presents the interferometry images themselves and central longitudinal 2D profiles. At both 6,500 cycles and 22,300 cycles, the wear volume of the steel counterparts used with the type B composite was larger, while the wear morphology of the steel was the same for both composites. These results indicate that the adhesion between the PA66 and GFs influences the aggressive effects of the GFs on the steel counterparts. In our previous work [19], we found that the wear volume of the steel counterparts increases when the GFs are oriented perpendicularly to the sliding surface compared to when they are oriented in the parallel direction. This is because the edges of the GF, which have a strong aggressive effect on the steel counterparts, are exposed more easily in this orientation. In addition, the wear mode of the steel counterparts is two-body abrasion rather than three-body abrasion, and the aggressive effects of GFs that remain adhered to the sliding surface are greater than those of GFs that have completely detached from the composite surface and are present as a contaminant in the grease. Therefore, the type B composite, with its lower interfacial shear strength between PA66 and the GFs, exhibited earlier interfacial peeling and gap formation between the PA66 and the GFs, and exposure of the GF edges occurred in earlier cycles, leading to the high wear volume of the steel counterparts.

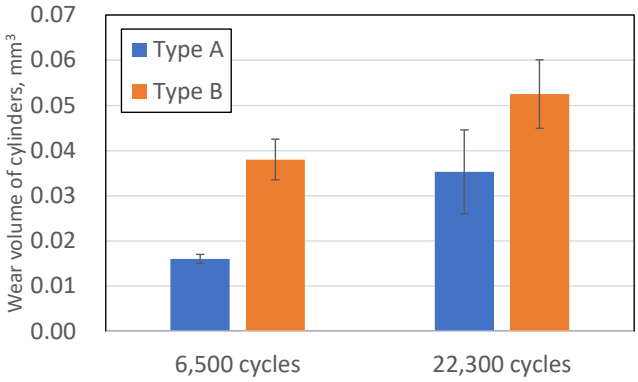

Fig. 7 Wear volume of the steel counterparts at different cycle numbers using composites that differed only in the GF surface treatment agent used.

Type of agent	Cycle numbers	Observation of wear scar	Central longitudinal 2D profile
Type A	6,500 cycles	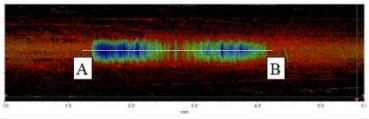	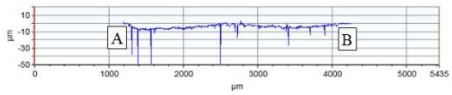
	22,300 cycles	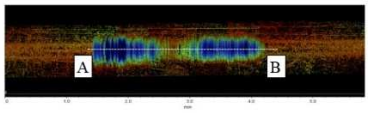	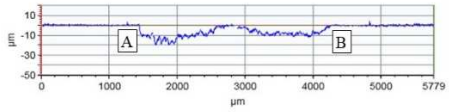
Type B	6,500 cycles	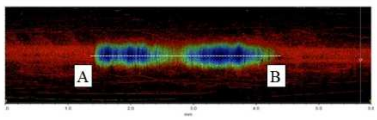	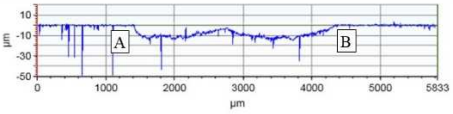
	22,300 cycles	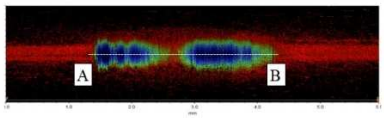	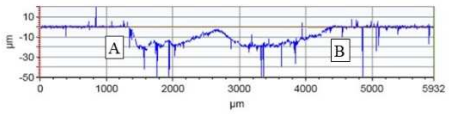

Fig. 8 Observation of the steel counterparts and central longitudinal 2D profiles using interferometry.

In order to discuss their aggressive effect on the steel counterparts, the orientation of the GFs on the composite surface was estimated using the surface image analysis method presented in Section **2.5**. Fig. 9 shows the total areas and perimeters of the GFs in the composites fabricated using the two GF surface treatment agents. The total area of the GFs treated with the type A surface agent was slightly larger than that of the GFs treated with type B, while no clear trend in the total perimeter of the GFs was observed. These results do not explain the different wear on the steel counterparts, because the wear in the tests using the type A composite, which had a larger total GF area on the sliding surface, was smaller than that in the tests using the type B composite. Fig. 10 shows the relationship between the circularity of the GFs and the cumulative frequency of the GF area, as well as the average value of C_{50} at different positions (C_{50} is the circularity value at which the cumulative GF area

frequency is 50%). The results indicate that the circularity at the center position was much lower than that at the inner/outer positions for both composites, indicating that the majority of the GFs at the center position were aligned parallel to the sliding direction. However, the relative orientations of the GFs at the inner, center, and outer positions was the same regardless of the type of surface agent used.

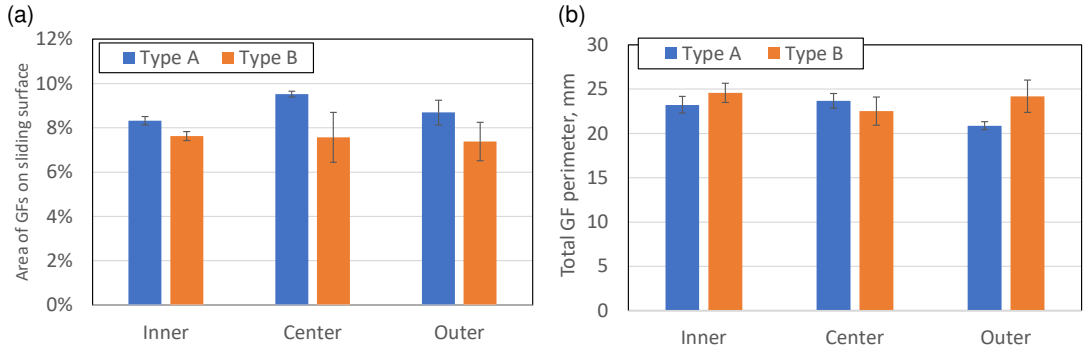

Fig. 9 (a) Calculated total area and (b) total perimeter of the GFs on composites that differed only in the surface treatment agent used. Three measurements were conducted at each position.

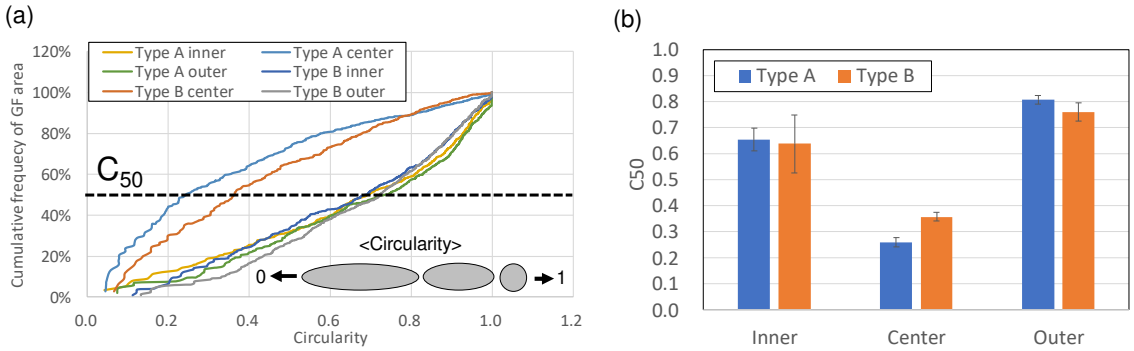

Fig. 10 (a) Relationship between the circularity of the GFs and the cumulative frequency of the GF area. (b) Value of C_{50} at the different positions of composite rings that differed only in the GF surface treatment agent used. Three measurements were conducted at each position.

In order to discuss the interfacial shear strength between the PA66 and GFs in the two composites quantitatively, a version of the Kelly–Tyson model was introduced [41] that was modified to consider the orientation of the reinforcement fibers [42, 43]. This model is frequently used to understand the mechanism of adhesion between resins and fibers, and takes into consideration the strength of the composite, fiber orientation, and fiber length distribution of the tensile specimens. The modified Kelly–Tyson model is presented below:

$$\sigma_t = f_0 \left\{ \sum_{l_i<l_c} \left(\frac{\sigma_f V_l l_i}{2l_c} \right) + \sum_{l_j>l_c} \left[\sigma_f V_j \left(1 - \frac{l_c}{2l_j} \right) \right] \right\} + \sigma_m (1 - V_f) \qquad (5)$$

where σ_t is the tensile strength of the composite, f_0 is the fiber orientation efficiency factor, σ_f is the strength of the fibers (3.2 GPa for E glass), σ_m is the tensile strength of the matrix resin (82 MPa for unreinforced PA66), l_c is the critical fiber length, l_i is a fiber length below the critical fiber length, l_j is a fiber length above the critical

fiber length, V_i and V_j are the fiber volume fractions of l_i and l_j, respectively, and V_f is the volume fraction of the fibers (7.3%). The fiber orientation can be measured through SEM image analysis, and the fiber orientation efficiency factor f_0 can be determined using the following equation:

$$f_0 = \sum_n a_n cos^4 \theta_n \qquad (6)$$

where a_n is the proportion of fibers that form an angle θ_n with respect to the flow direction of injection molding as presented in Fig. 11. The critical fiber length l_c is defined as the minimum fiber length necessary for the fiber stress to reach the maximum strength of the fiber σ_f at the fiber ends [43]. The interfacial shear strength τ can be calculated using the following equation:

$$l_c = \frac{\sigma_f d}{2\tau} \qquad (7)$$

where d is the fiber diameter (6.5 μm). Therefore, the interfacial shear strength τ can be estimated using the values of the fiber orientation efficiency factor f_0 and critical fiber length l_c using equations (5), (6), and (7).

The fiber length distribution of the GFs in the tensile test specimens was measured through the following process. First, 30 mg of the molding of the composite was cut from the center position of the specimens (Fig. 12). This fragment was then combusted using a TG-DTA (thermogravimeter-differential thermal analyzer) at 650 °C for 2 h, and the residual GFs were retrieved. Finally, the length distribution of the GFs (total number: 425–912) with a length of 0.07 mm or greater was measured automatically using an optical microscope and image analysis software. Fig. 13 presents the relationship between the length and cumulative frequency of the length of the GFs from the composites prepared using the two surface treatment agents. No significant differences in their fiber length distributions were observed, and the number average fiber lengths of the type A and type B composites were 0.199 mm (+/- 0.005 mm) and 0.210 mm (+/- 0.001 mm), respectively. The similar fiber length distributions were attributed to the fact that these two GF-based composites were fabricated using PA66 with the same molecular mass, the same amount of GFs, and the same GF diameter through the same extrusion and injection molding process. These results indicated that the surface treatment agent did not affect the fiber length distribution. The fiber orientation efficiency factor f_0 was then estimated using the following process. First, the test specimen was embedded in epoxy resin and cured. Then, specimens with 4 mm thickness of the skin layer (0.3 mm depth from the top surface of the specimen) and core layer (2 mm depth from the top surface of the specimen) surfaces were obtained by polishing, as presented in Fig. 12. Subsequently, each surface was observed using SEM in BSE mode to obtain images of the GF orientation, which are presented in Fig. 14. The average orientation angle θ relative to the base axis (direction of the tensile test) was estimated by image analysis of the binarized images using the software package image J. Image analysis was conducted using six SEM images with different fields of view; as in the fiber length measurement, only fibers with a length of over 0.07 mm were analyzed. The transverse direction is the direction of the injection molding and of the tensile test. Fig. 15 shows the relationship between the orientation angle θ and the cumulative frequency of the GF orientation. As in the fiber length distribution, no significant difference in GF orientation was observed between

the samples prepared using the different surface treatment agents on either the core or skin surface. The average orientation angles θ for the type A composite were 17.6° (core surface) and 14.3° (skin surface), while those of the type B composite were 13.6° (core surface) and 16.5° (skin surface).

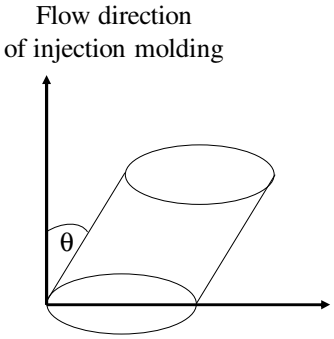

Fig. 11 Fiber orientation angle θ_n [43].

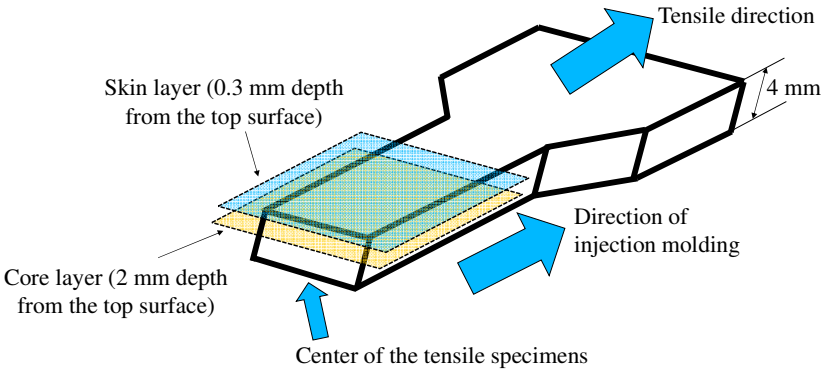

Fig. 12 Image of the tensile test specimens.

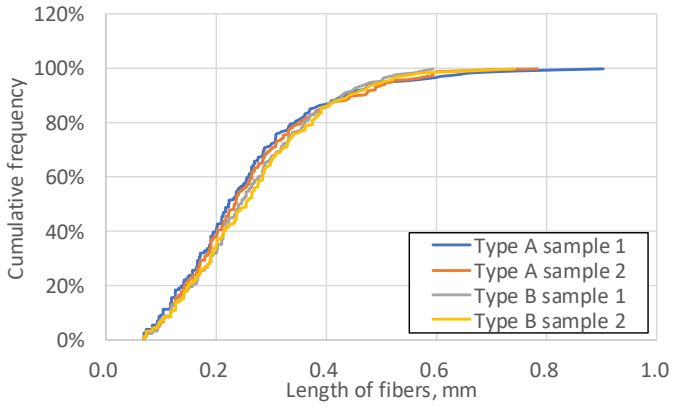

Fig. 13 Relationship between the GF length and the cumulative frequency of GFs for composites that differed only in the surface treatment agent used.

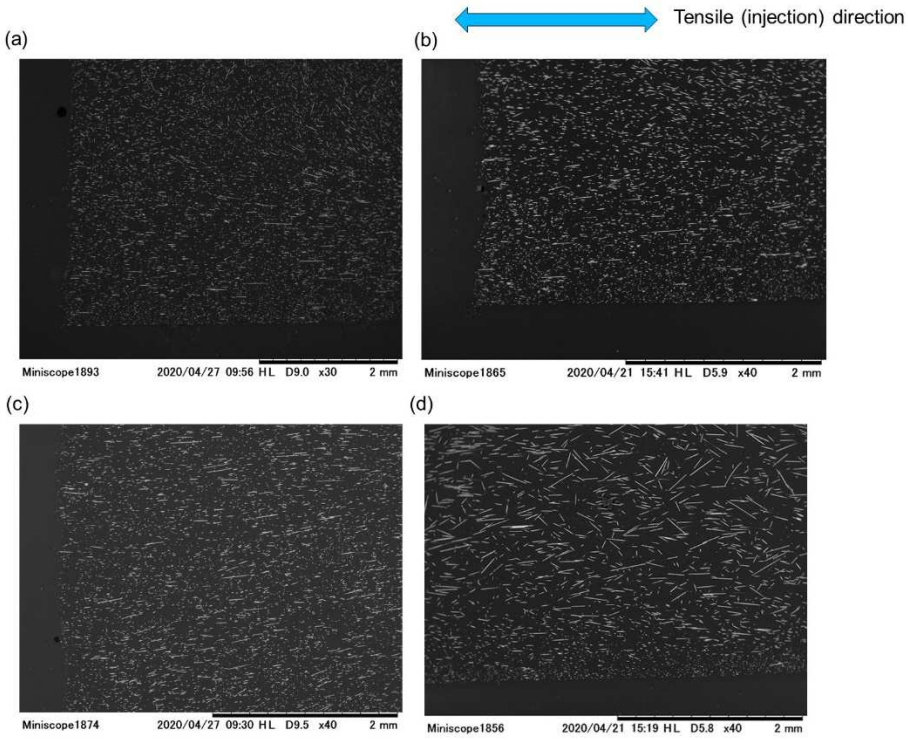

Fig. 14 SEM observations of the tensile specimens: (a) Type A composite core layer; (b) type A composite skin layer; (c) type B composite core layer; (d) type B composite skin layer.

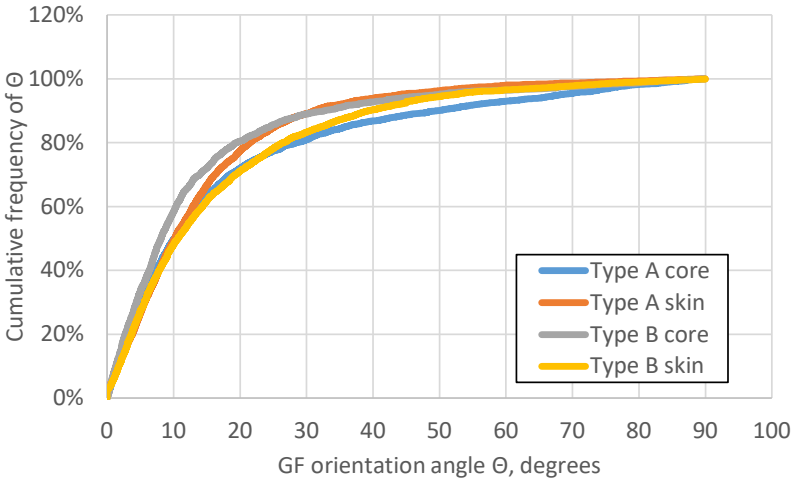

Fig. 15 Relationship between the GF orientation angle and the cumulative frequency of the GF orientation on the surfaces of composites that differed only in the GF surface treatment agent used.

Table 7 lists the estimated fiber angle relative to the injection (tensile) direction (θ_n, average values for the core layer and skin layer), the fiber orientation efficiency factor f_0 estimated from equation (6), and the critical fiber length l_c estimated from equation (5) for the composites prepared using the two surface treatment agents. The critical fiber length l_c for the type A composite was lower than that of the type B composite, which indicates that when the type A agent is used, many more fibers contribute to building up the axial fiber stress to the maximum strength of the fiber σ_f at the fiber ends than when the type B agent is used.

Based on the obtained values, the interfacial shear strength τ was estimated using equation (7), these values are also listed in Table 7. The τ values of the type A and type B composites were 33.6 +/- 0.8 MPa and 25.7 +/- 0.5 MPa, respectively, i.e., the interfacial shear of the type A composite was 7.9 MPa (30.6%) higher than that of the type B composite. These values are similar to those previously reported for PA/GF composites (39–40 MPa [32], 24.0 MPa [42], and 33.5–48.4 MPa [44]). Therefore, the interfacial shear strengths of the tensile test specimens exhibited the expected tendency based on the results of the sliding test and the SEM images of the sliding surfaces.

Table 7 Estimated values of θ_n, f_0, l_c, and τ for composites that differed only in the GF surface treatment agent used.

	θ_n	f_0	l_c	τ
Type A	16.0° (0.278 rad)	0.855	0.305 mm	33.6 +/- 0.8 MPa
Type B	15.0° (0.262 rad)	0.870	0.410 mm	25.7 +/- 0.5 MPa

3.2 Effects of the molecular mass of PA66 on the mechanical and tribological properties

The effects of the molecular mass of PA66 on the mechanical and tribological properties of the GF-reinforced PA66 composites were evaluated using composite samples that were prepared using PA66 matrices with four different molecular mass values (samples 1, 3, 4, and 5, see Table 5). These samples contained the same type and content of GFs (surface treatment agent: type A, GF diameter: 6.5 μm, GF amount: 15 wt%). Fig. 16 shows the wear and creep height losses of these composites after various numbers of sliding test cycles; the wear and creep height losses were calculated individually as detailed in Section **2.1**. The results indicated that the wear or creep at a given cycle number decreased with increasing molecular mass of the PA66 composite. This tendency in the wear resistance is the same as the one observed in [30] which used the GF or aramid fiber reinforced PA66 under grease lubrication in which the molecular mass of PA66 was increased through the reactive extrusion using poly- carbodiimide additives. Fig. 17 presents the evolution of the friction coefficient, temperature, and vertical displacement with the cycle number. The sudden increases in the friction coefficient, temperature, and vertical displacement were observed at later cycle numbers for the composites with greater PA66 molecular mass values; for example, a sudden increase in the vertical displacement occurred at 22,000 cycles for the composite with a VN of 145 ml/g, 80,000 cycles for the 193 ml/g composite, and 125,000 cycles for the 235 ml/g composite, whereas no increase in the vertical displacement was observed until 140,000 cycles for the composite with a VN of 356 ml/g.

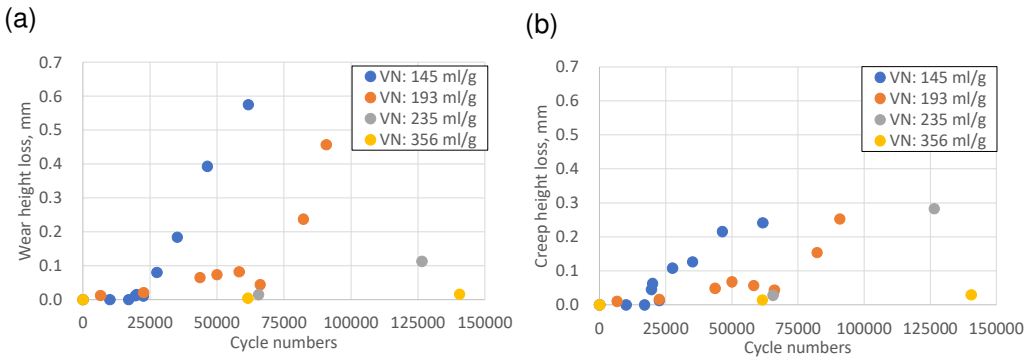

Fig. 16 (a) Wear height loss and (b) creep height loss as a function of the cycle number in sliding tests of GF-reinforced composites that differed only in their PA66 molecular mass (VN).

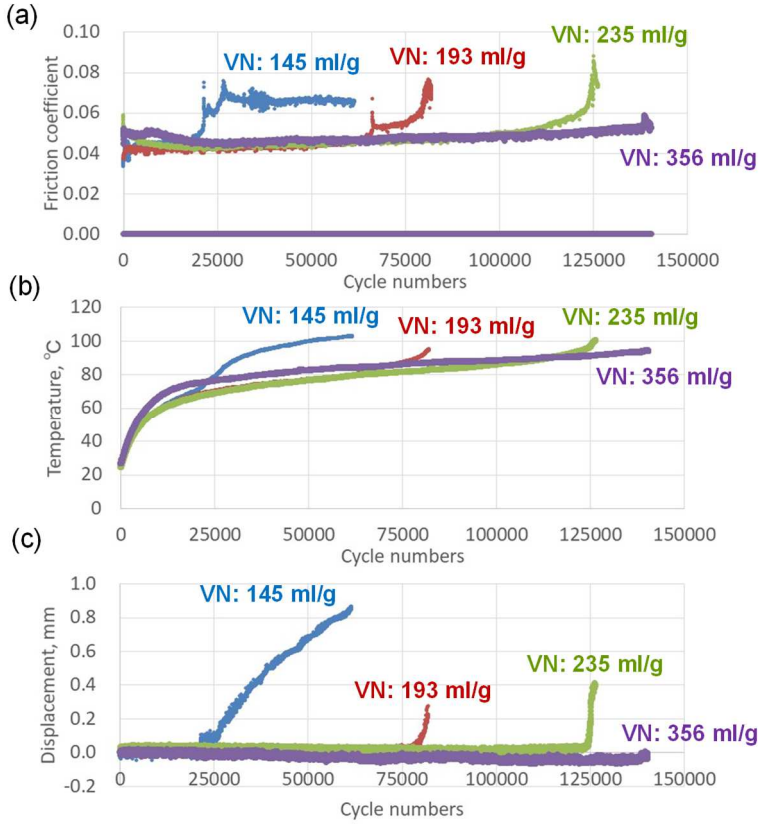

Fig. 17 Evolution of (a) the friction coefficient, (b) temperature, (c) and vertical displacement with cycle number in the sliding tests of composites that differed only in their PA66 molecular mass (VN).

.

Fig. 18 shows the optical microscope and SEM images of the sliding surfaces of the 145 ml/g and 193 ml/g composites after 22,500 cycles. Peeling was observed at the center region of the 145 ml/g composite. Additionally, scratching of the PA66 and several holes related to detached GFs were observed via SEM, even in regions of the surface where peeling was not observed in the optical microscope images. In contrast, no severe peeling or damage was observed on any part of the sliding surface of the 193 ml/g composite.

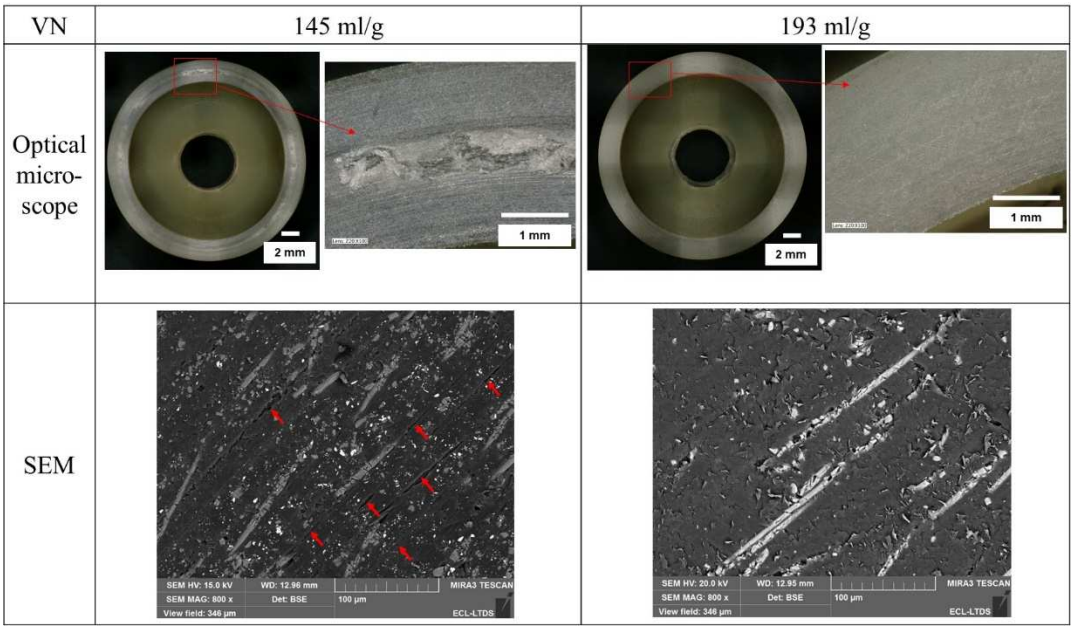

Fig. 18 Optical microscope and SEM images of the sliding surfaces of composites that differed only in their PA66 molecular mass (VN) after 22,500 cycles.

To study the wear phenomena of the composite samples with high VN values (>145 ml/g), longer tests were conducted. Fig. 19 presents the optical microscope and SEM images of the sliding surfaces of the 145 ml/g composite after 61,500 cycles and those of the 193 ml/g and 235 ml/g composites after 65,500 cycles, along with the wear and creep height loss after each test. In contrast to the limited wear observed after 22,500 cycles, the entire sliding surface of the 145 ml/g sample was worn after 61,500 cycles, and severe peeling of the PA66 resin was observed via SEM. The wear height loss was greater than the creep height loss. In the case of the 193 ml/g sample, peeling of the center region and hole formation on the composite surface were observed after 65,500 cycles. In contrast, no severe peeling was observed on any part of the sliding surface of the 235 ml/g composite after 65,500 cycles, although weak sliding marks were present. The wear height losses of the 193 ml/g and 235 ml/g samples were significantly lower than that of the 145 ml/g sample. The creep height losses of these high-molecular-mass samples were greater than their wear height losses; however, their creep values were much lower than that of the 145 ml/g sample. Consequently, increasing the molecular mass of PA66 was concluded to decrease the damage to the sliding surface, leading to improved wear and creep resistance in the composites.

VN	145 ml/g (61,500 cycles)	193 ml/g (65,500 cycles)	235 ml/g (65,500 cycles)
Optical micro-scope	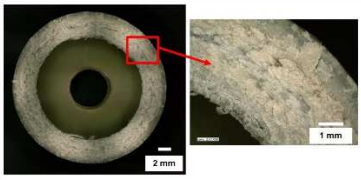	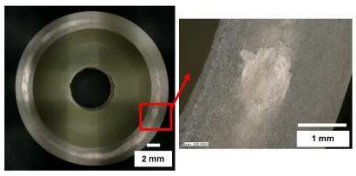	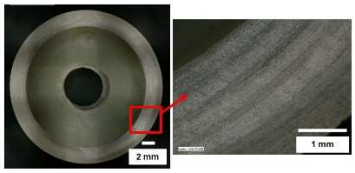
SEM	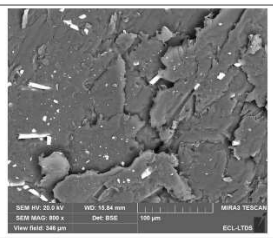	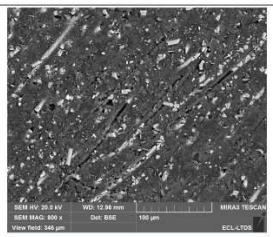	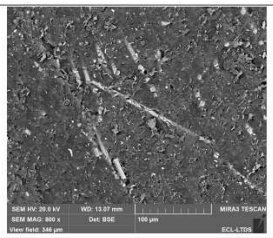
Wear height	0.575 mm	0.001 mm	0.015 mm
Creep height	0.242 mm	0.043 mm	0.028 mm

Fig. 19 Optical microscope and SEM images of the sliding surfaces of composites that differed only in their PA66 molecular mass (VN) after 61,500–65,500 cycles.

The effect of the molecular mass of the PA66 on the wear resistance of the steel counterparts was also investigated. Fig. 20 shows the wear volume of the steel counterparts (total wear volume of the four steel cylinders, measured using interferometry) after different numbers of sliding test cycles with the composite samples with different molecular masses of PA66. The wear volume of the steel counterparts increased proportionally with increasing cycle number. Similarly to the wear resistance of the composite, the wear of the steel counterparts also decreased with increasing PA66 molecular mass for any given cycle number. This indicates that not only the wear and creep resistance of the composite, but also the wear resistance of the steel counterparts, are improved by increasing the molecular mass of the PA66 in the composite. In our previous study [19], the wear mode of the steel counterparts was reported to be two-body abrasion caused by the GFs on the surface of the composite. This was confirmed in the current study by comparing the wear rate and mode of the steel counterpart using new grease and contaminated grease (grease containing wear debris accumulated over 61,500 cycles under the same test conditions) in 61,500 cycle sliding tests with composite sample 3, as shown in Fig. 21. Therefore, the mechanism by which the use of higher-molecular-mass PA66 in the composite decreases its aggressive effect on the steel counterpart via this wear mode is discussed later in this section in terms of the GF orientation on the sliding surface and mechanical properties of the composite.

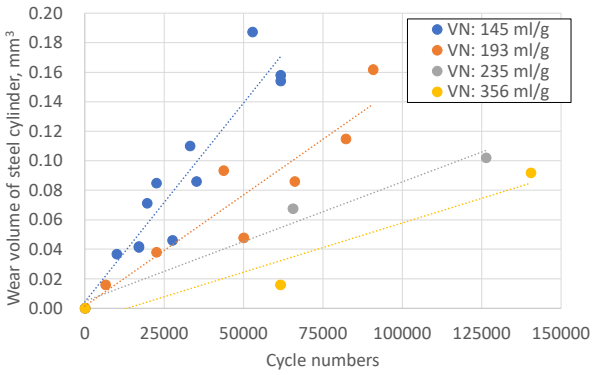

Fig. 20 Wear volume of the steel cylinders after different cycle numbers of the sliding test using composites that differed only in their PA66 molecular mass (VN).

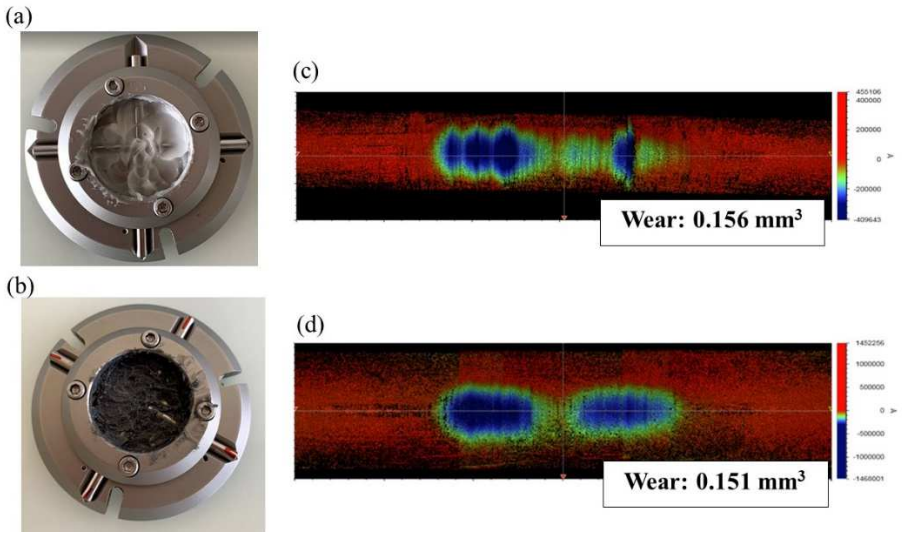

Fig. 21 Photographs of (a) new grease and (b) contaminated grease, and interferometry measurements of the steel counterpart after sliding tests using the (c) new grease or (d) contaminated grease [19].

The effect of the fiber distribution and orientation on the sliding surface was summarized quantitatively to discuss the aggressive effects of the reinforcement fibers to the steel counterpart. Fig. 22 shows the results of image analysis (calculated total GF areas, total GF perimeters, relationship between the GF circularity and cumulative area, and average value of C_{50}) at different positions of the composite rings with different PA66 molecular mass values. Image analysis was conducted as described in Section **2.5**. No significant differences among the GF areas or total perimeters were observed at the different positions, nor was a significant difference in the circularity (GF orientation) observed between composites with different molecular masses for a given position on the composite ring. These results demonstrate that the effect of the PA66 molecular mass on the wear or creep resistance of the composite and the wear resistance of the steel counterpart cannot be explained in terms of the orientation of the GFs relative to the sliding surface.

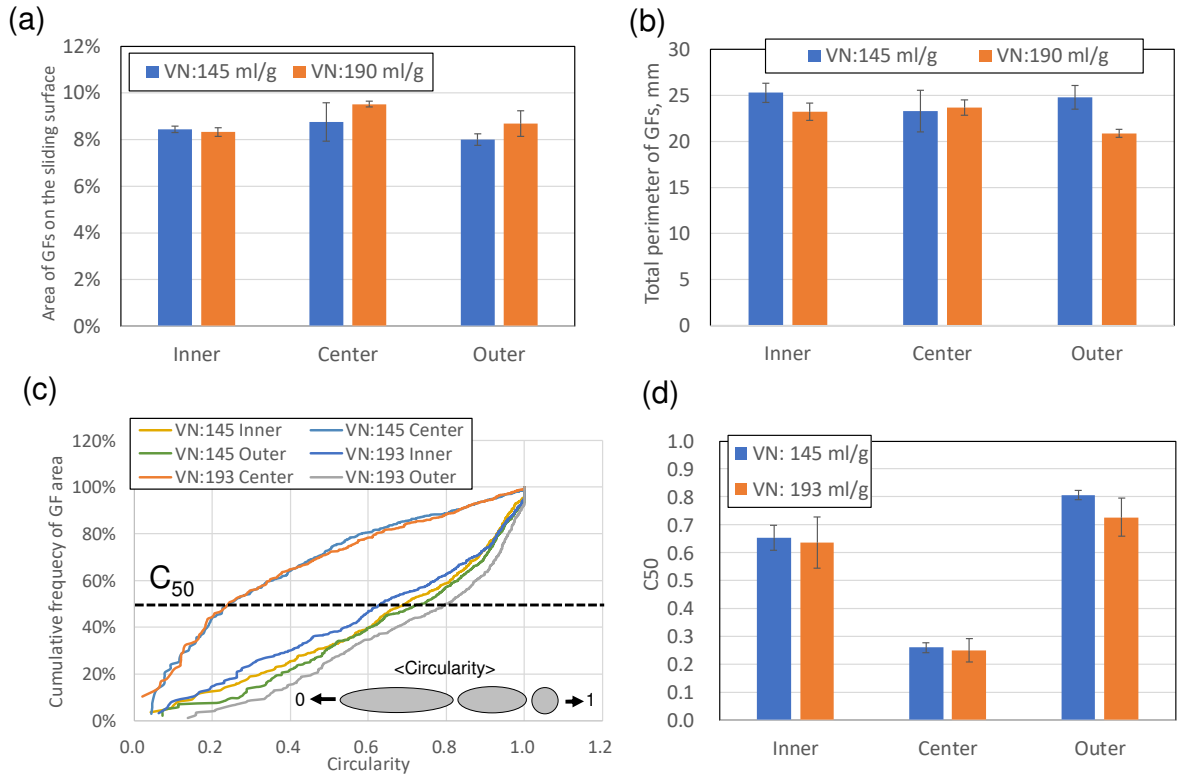

Fig. 22 (a) Total GF area; (b) total GF perimeter; (c) relationship between the circularity of the GFs and the cumulative frequency of GF area; (d) value of C_{50} at different positions of composite rings that differed only that differed only in their PA66 molecular mass (VN). Three measurements were conducted at each position.

To discuss the reason why the increase in the molecular mass of the PA66 can reduce the wear of the steel counterpart, the effect of the mechanical properties of the PA66 or composite was investigated. Fig. 23 shows the Young's modulus and the hardness at the surfaces of the composite rings fabricated using PA66 with two different molecular mass values, which were measured using micro-indentation. No differences between the Young's moduli or hardness values of the samples were observed, which indicated that the PA66 molecular mass did not affect the elasticity or plasticity of the composite. Based on these results, we then focused on the toughness of the PA66 as a possible origin of the effect of its molecular mass on the wear resistance of the steel counterpart and composite. Evaluation of the toughness of the composite using the composite rings (sliding test specimens) was difficult. Therefore, the toughness of the composites was evaluated using tensile test samples from the tensile elongation at break or tensile breakage energy. Fig. 24 presents the stress–strain curves obtained in the tensile tests using unreinforced PA66 samples with different molecular mass values (raw PA66 of composite sample 3 (VN: 150 ml/g) and 4 (VN: 302 ml/g)). Although their Young's moduli in the initial stage of the test and their yield strength values were very similar, the elongation at break of the high-molecular-mass PA66 sample was 3.5 times higher than that of the normal-molecular-mass sample. This result indicates that increasing the molecular mass of PA66 does not improve its strength and stiffness, but does greatly improve its toughness. Additionally, the effect of the molecular mass of PA66 on the tensile mechanical properties of the

GF-reinforced PA66 composites were investigated. Fig. 25 shows the stress–strain curves obtained in tensile tests using GF-reinforced PA66 composite samples with different PA66 molecular masses (samples 1, 3, 4, and 5). Fig. 26 shows the relationship between the PA66 molecular mass of the GF-reinforced PA66 samples and their tensile mechanical properties. Similarly to in the case of the unreinforced PA66, and as observed in the mechanical properties of the composite with added poly-carbodiimide which presented high molecular mass of the PA66 [30], the molecular mass of PA66 had only a weak influence on the tensile strength and Young's modulus (confirming the micro-indentation results); however, the toughness (tensile elongation at break and tensile breakage energy) increased with the molecular mass.

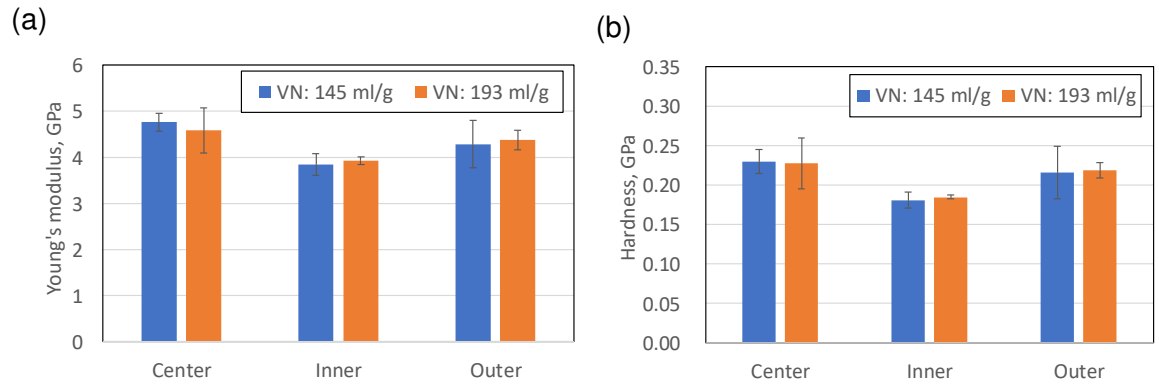

Fig. 23 (a) Young's modulus and (b) hardness of the sliding surfaces of composite rings that differed only in their PA66 molecular mass (VN). Three measurements were conducted at each position.

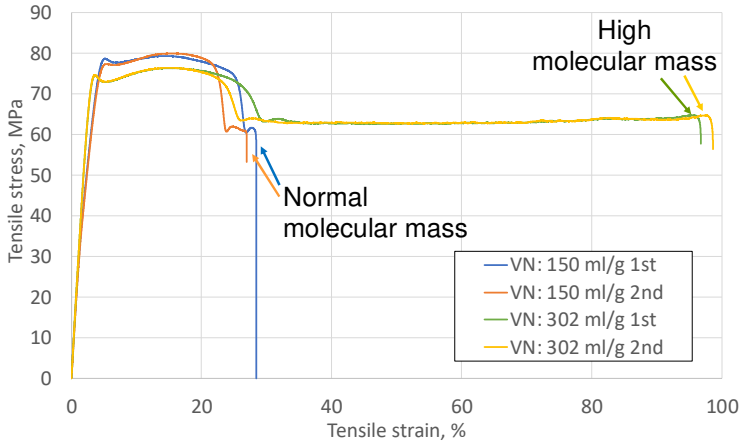

Fig. 24 Stress–strain curves from the tensile tests of unreinforced PA66 samples with different molecular mass values.

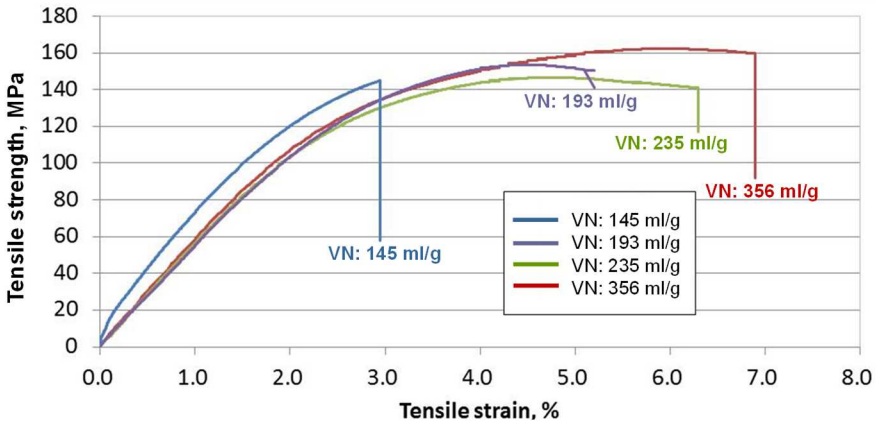

Fig. 25 Stress–strain curves from the tensile tests of GF-reinforced composites that differed only in their PA66 molecular mass (VN).

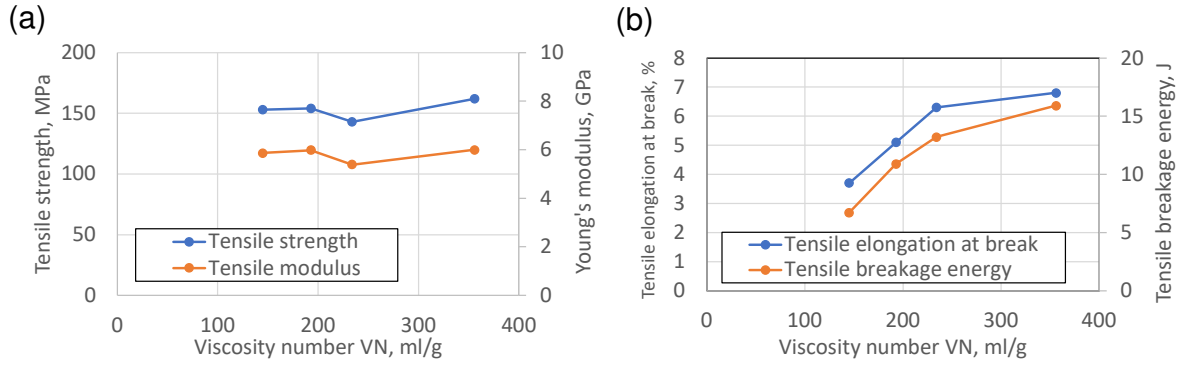

Fig. 26 Relationship between the VN of the composite and the (a) tensile strength and Young's modulus and the (b) tensile elongation at break and tensile elongation energy.

Given these results, we propose a mechanism to explain the effect of the molecular mass of PA66 on the wear of the steel counterpart and the composite. The interfacial shear strength between PA66 and GF should be the same in the composites with different PA66 molecular masses (i.e., samples 1, 3, 4, and 5) because the same GF surface treatment agent was used in their preparation, and the differences among their tensile strengths were small. In contrast, the elongation of the PA66 resin due to its shear strength increases with its molecular mass, and thus, the resin can more easily follow the deformation of the fibers due to the local shear induced by sliding. Consequently, fewer interfacial gaps between PA66 and the GFs are generated during sliding. This reduces the exposure of GF edges, which have a highly aggressive effect on the steel counterpart, which in turn reduces the two-body abrasive wear of the steel counterpart. Additionally, the propagation of the scratching of PA66, which originates from gaps between PA66 and GF, is reduced due to the high toughness of the high-molecular-mass polymer. Fig. 27 illustrates the different wear modes during sliding contact for composites with different PA66 molecular masses. As shown, the damage to the sliding surface is decreased, as presented in Fig. 18 and 19, and the wear and creep of the composite are reduced.

In terms of practical application, these results suggest that a composite worm gear in contact with a steel worm shaft could be fabricated using a GF-reinforced PA66 composite with a high PA66 molecular mass. This would obviate the need for expensive heat treatment of the steel to increase its hardness and wear resistance, as

the higher molecular mass composite would reduce the wear of both the soft steel and the composite. The use of soft steel would also permit easy machining of the teeth via mechanical cutting.

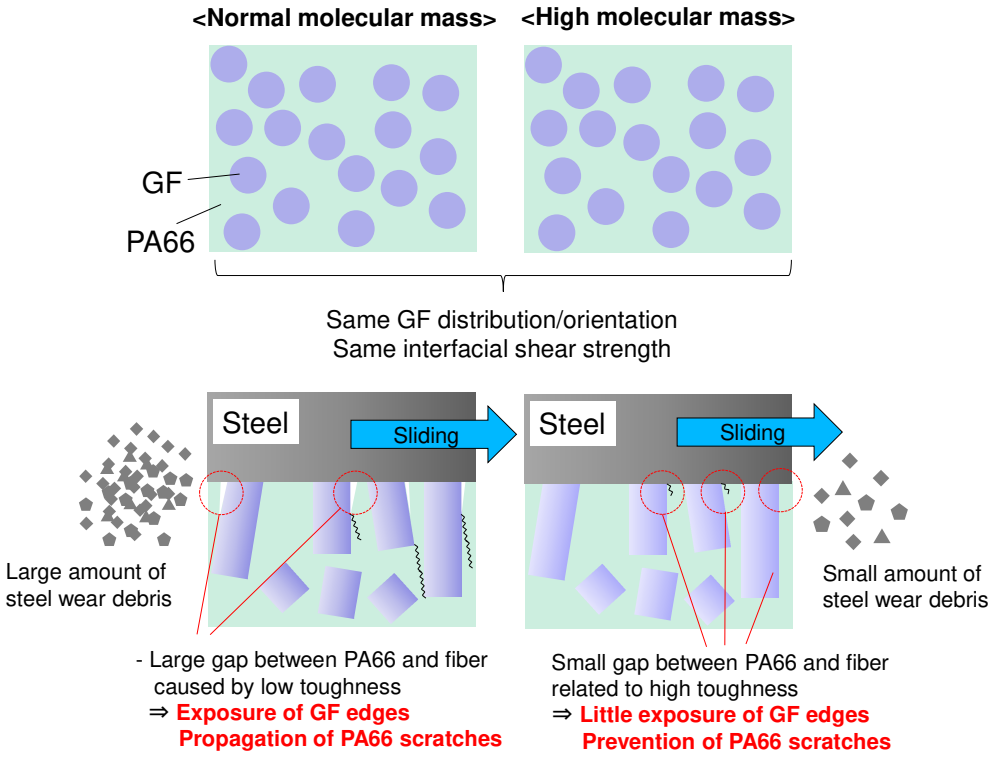

Fig. 27 Schematic of the different wear modes of composites with different PA66 molecular mass values.

3.3 Effects of GF diameter on the mechanical and tribological properties

In order to investigate the effects of the GF diameter, composite samples containing GFs of different diameters were prepared. In these samples, the molecular mass of the raw PA66, the GF surface treatment agent (type A), and the GF content (15 wt%) were the same. First, the effect of the GF diameter on the tensile mechanical properties was investigated. Fig. 28 shows the tensile mechanical properties of these composites. The tensile strength increased with decreasing GF diameter; the tensile strength of the composite containing 6.5 μm diameter GFs was 38.1 MPa (32.9%) higher than that of the composite with 19 μm GFs. The tensile elongation at break and tensile breakage energy also increased with decreasing GF diameter. The tensile elongation at break and tensile breakage energy of the composite with 6.5 μm GFs were 1.90 and 2.72 times higher than those of the composite with 19 μm GFs, respectively. In contrast, the Young's moduli of the composites were not affected by the GF diameter. Thus, the GF diameter affected only the mechanical properties related to irreversible deformation (plasticity and breakage) of the composite. The increased interfacial area between the GFs and PA66 in the smaller-diameter GFs allows them to bear higher stress without breaking; these results are in agreement with those presented in previous studies [32-34], as explained in Section **1**.

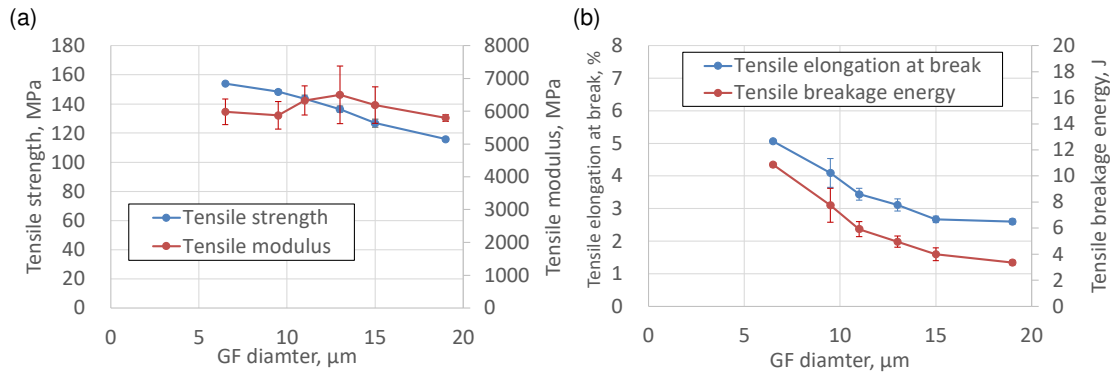

Fig. 28 Tensile mechanical properties of GF-reinforced PA66 composites that differed only in GF diameter. (a) Tensile strength and Young's modulus; (b) tensile elongation at break and tensile breakage energy. Each value is the average value of five measurements.

Next, the effect of the GF diameter on the tribological properties was investigated. Fig. 29 shows the evolution of the friction coefficient, temperature, and vertical displacement of the composite samples with different GF diameters during the sliding tests; the tests were stopped at 50,000 cycles. The friction coefficient increased with increasing GF diameter. The friction coefficient of the composite with 6.5 μm GFs remained low throughout the 50,000 cycles, and no sudden increase in its value was observed. The composites with GF diameters of 9.5, 13, and 19 μm did exhibit sudden friction coefficient increases; these sudden increases occurred at earlier cycle numbers with increasing GF diameter. The rate of temperature increase corresponded to the friction coefficient for each GF diameter, and the temperature increased with increasing GF diameter. No sudden increase in the displacement was observed during the 50,000 cycles for the composite with a GF diameter of 6.5 μm. In contrast, sudden increases in displacement were observed for the 9.5, 13, and 19 μm GF samples at the same cycle numbers as the sudden increases in the friction coefficient. Fig. 30 shows optical microscope images of the sliding surfaces after 50,000 cycles. No severe peeling was observed on the sliding surface of the composite with a GF diameter of 6.5 μm. In contrast, evident peeling occurred at the center region of the composite rings with GF diameters of 9.5, 13, and 19 μm. This difference was attributed to the decreased strength and toughness of the samples with larger GF diameters, which could accelerate the damage on the sliding surface. The plastic deformation (sudden increase in the displacement) and peeling on the sliding surface were believed to occur via the mechanism of sliding surface damage reported in our previous study [19].

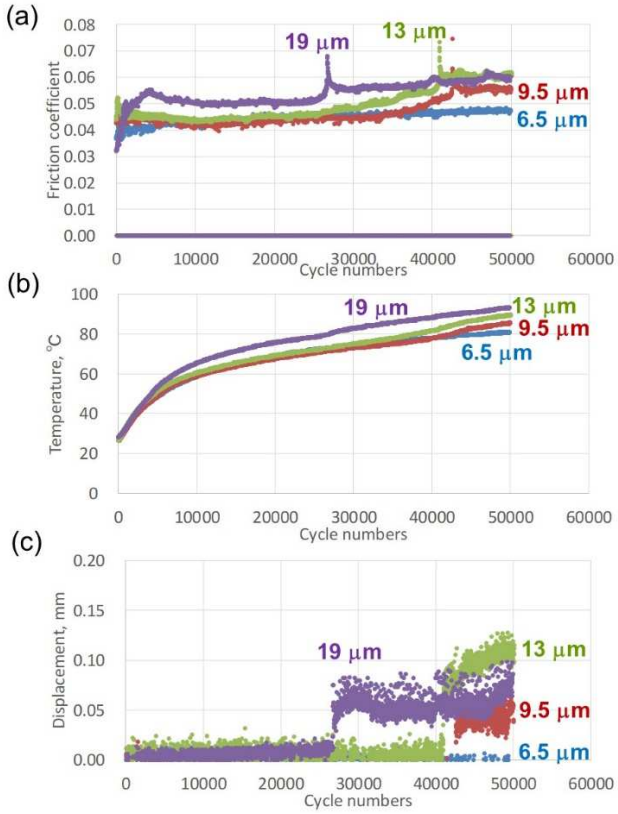

Fig. 29 Evolution of (a) the friction coefficient, (b) temperature, and (c) vertical displacement of composites that differed only in GF diameter during a 50,000 cycle sliding test.

Diameter	6.5 μm	9.5 μm	13 μm	19 μm
Magnification ×20	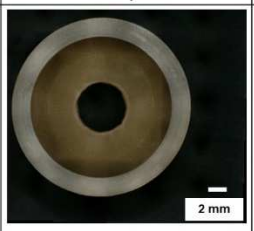	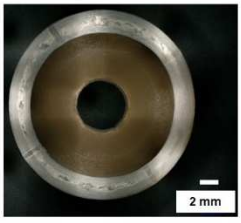	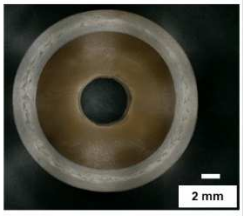	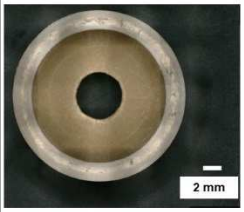
Magnification ×100	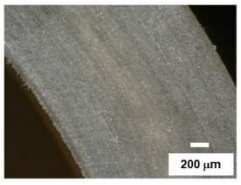	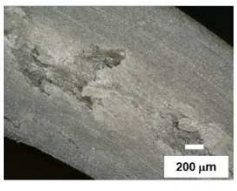	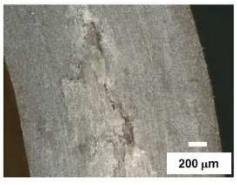	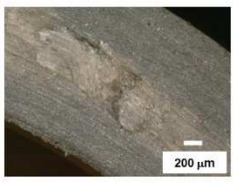

Fig. 30 Optical microscope images of the sliding surfaces of the composites with different GF diameters after 50,000 cycles.

Fig. 31 shows the evolution of the friction coefficient, temperature, and vertical displacement of the composite samples containing GFs of different diameters during longer sliding tests. Similarly to in the 50,000 cycle tests, the friction coefficient and temperature were lower for samples with smaller GF diameters.

Additionally, the sudden increases in the friction coefficient and vertical displacement occurred earlier for samples with larger GF diameters. The same pattern was observed for the increase in the displacement. For the composite with a GF diameter of 6.5 μm, the displacement increased suddenly at 66,000 cycles and then remained nearly constant until 80,000 cycles, after which it increased rapidly. In comparison, the rates of increase in the displacement were smaller for the composites with GF diameters of 9.5 μm or 13 μm. Fig. 32 presents the relationship between the GF diameter and the cycle number at which the first sudden increase in the friction coefficient occurred; these data were fitted using a power approximation. The same tendency was observed as in the 50,000 cycle test; i.e., the cycle number at which the first sudden increase in the friction coefficient occurred increased with decreasing GF diameter. Additionally, for the composite with 19 μm GFs, the rate of the increase in the displacement was much lower than that of the 9.5 μm and 13 μm GF samples. The absolute value of the displacement was also lower, despite the fact that the first sudden increase in the friction coefficient and displacement occurred at a lower cycle number. Hence, the order of the absolute values of the displacements of the samples with different GF diameters varied at different cycle numbers.

The changes in the order of the displacement values were related to the difference in contact pressure due to the wear of the steel cylinders. Fig. 33 presents the wear volume of the steel counterparts tested using composites with different GF diameters after different cycle numbers. Linear fitting of this data indicated that the wear of the steel cylinders increased proportionally with the cycle number; the fitting equations had high correlation coefficient values. The results also show that the wear of the steel counterpart increased with the diameter of the GFs. The wear volume on the steel using the 19 μm diameter GF composite was 3–6 times larger than that observed using the 6.5 μm diameter GF composite. Therefore, as the wear on the steel cylinders increases, the contact pressure becomes lower, which should reduce the rate of increase in the displacement (i.e., wear and creep of the composite). Summarizing the above, the use of small-diameter GFs is not usually effective to reduce the wear and creep of the composite over the entire sliding duration.

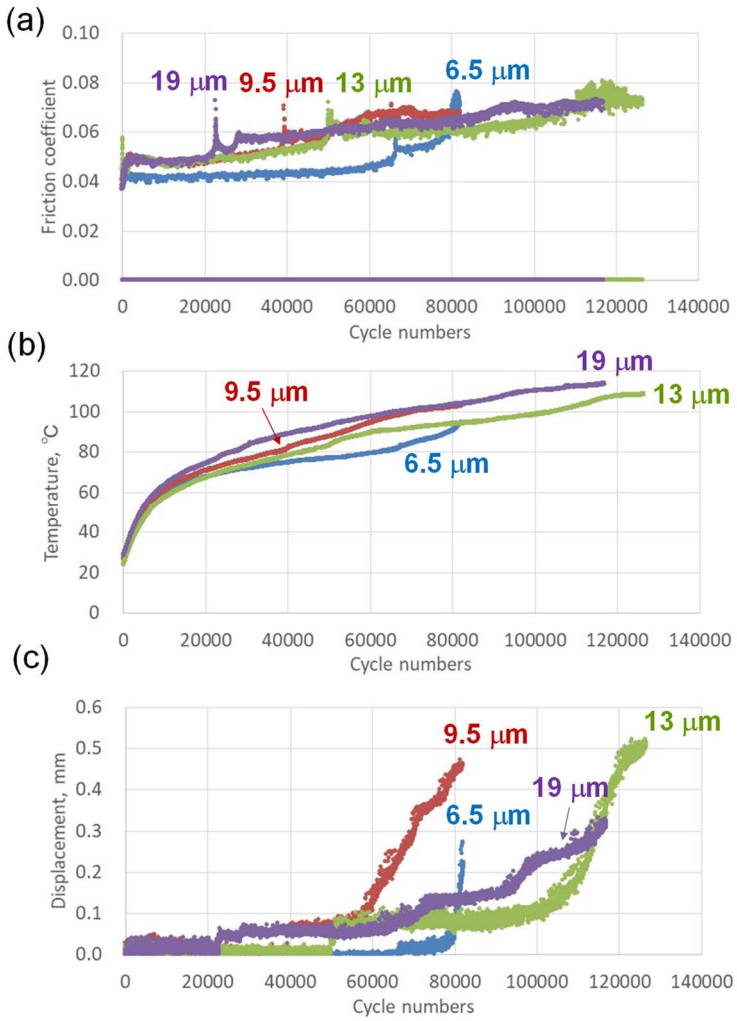

Fig. 31 Evolution of (a) the friction coefficient, (b) temperature, (c) and vertical displacement of composites that differed only in GF diameter in the longer sliding test.

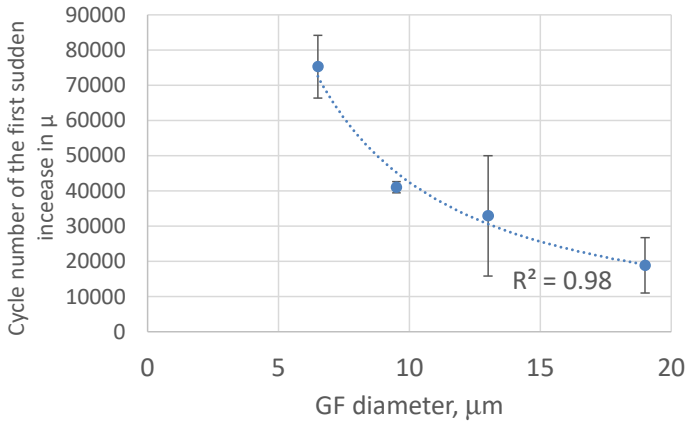

Fig. 32 Relationship between the GF diameter and the cycle number at which the first sudden increase in the friction coefficient occurred. Each value is the average value of three values.

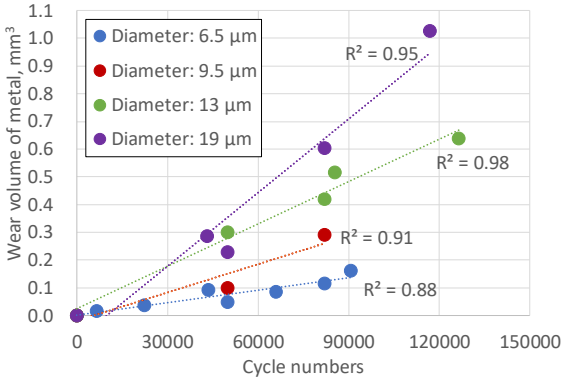

Fig. 33 Wear volume of the steel cylinders at different cycle numbers for composites that differed only in GF diameter.

In order to clarify the mechanism by which GFs with a larger diameter accelerated the wear of the steel cylinders, the orientation of the GFs on the sliding surfaces of the composite ring before the sliding tests was investigated using image analysis. Fig. 34 shows the surface images of the composite rings with different GF diameters after being polished with #4000 abrasive paper. Image analysis was conducted at three different locations at each of the three positions (inner, center, and outer) of the sliding surface of the composite rings (36 images total) as described in Section **3.1**. Fig. 35 shows the C_{50} values of the composites with different GF diameters at each position. The C_{50} values at the center positions were lower than those at the inner or outer positions, regardless of the GF diameter. This indicates that the GFs in the center region of the sliding surface were oriented more perpendicularly than those in the inner or outer regions. Additionally, the C_{50} values at the outer position tended to be higher than those at the inner position regardless of the GF diameter. This was attributed to the resin flow inside the metal die, which is determined by the injection molding conditions and the structure of the metal die [19]. The C_{50} values at each position can explain the differences in the wear of the steel cylinders at different positions. Fig. 36 shows interferometry measurements of the steel cylinders after 50,000 cycles after the removal of cylindrical shape and central longitudinal 2D profile. The wear volumes of the steel cylinders at positions corresponding to the inner, center, and outer positions of the composite ring were estimated, and are presented in Fig. 37a. Fig. 37b presents the relationship between the C_{50} values on the sliding surface of the composite and the wear of the steel cylinders at each position. The C_{50} values correlated well with the wear of the steel cylinders after the sliding tests with the composites with different GF diameters, which indicated that the wear volume at each position of the steel cylinders could be explained by the fiber orientation on the surface of its GF composite ring counterpart. However, the overall trend of the GF orientation was the same regardless of the GF diameter; thus the effect of the diameter of the GFs on the wear of the steel cannot be explained by the fiber orientation.

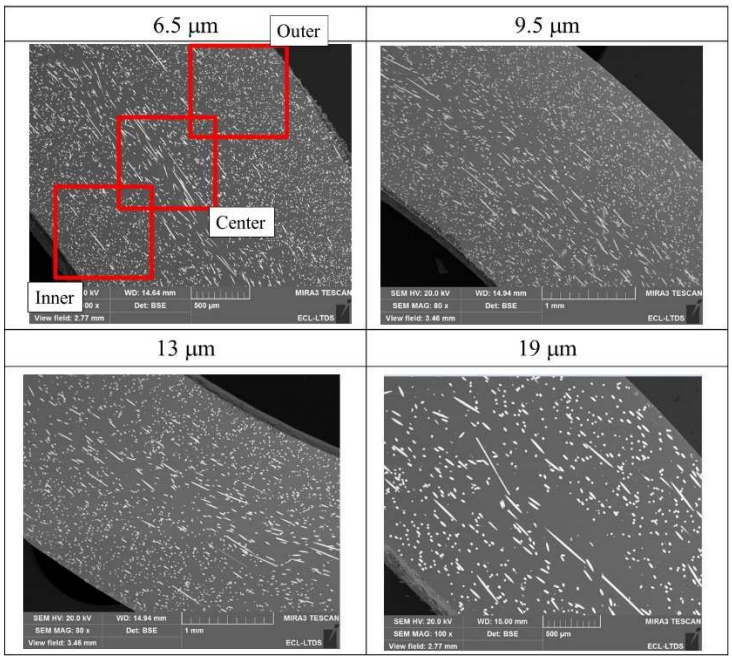

Fig. 34 SEM images of the surfaces of the composite rings with different GF diameters before the sliding tests.

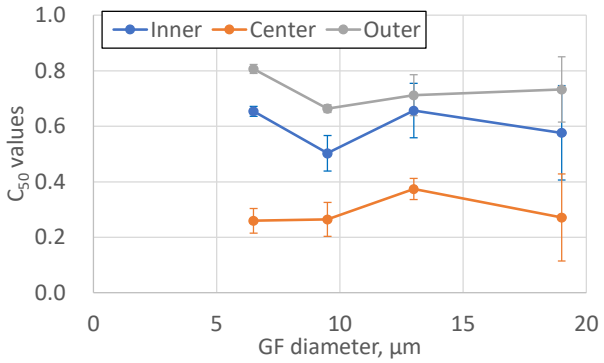

Fig. 35 C_{50} values at different positions of the surface of the composites with different GF diameters. Three measurements were conducted at each position.

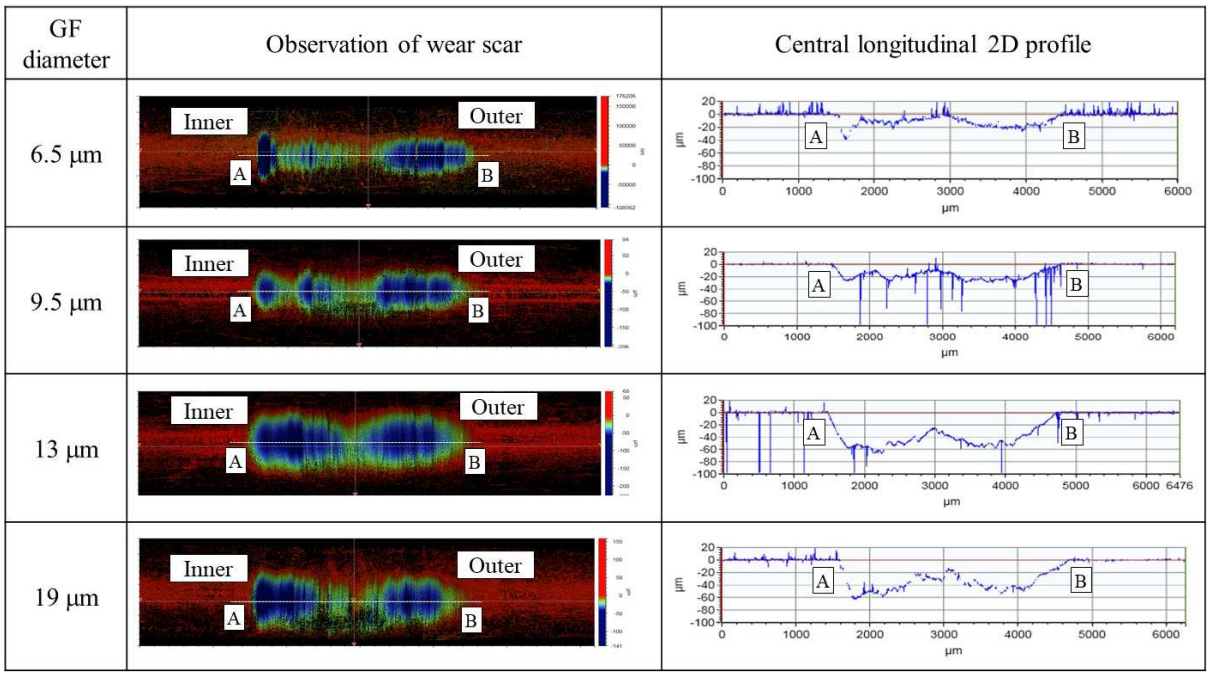

Fig. 36 Observation of the steel counterparts and central longitudinal 2D profiles using interferometry.

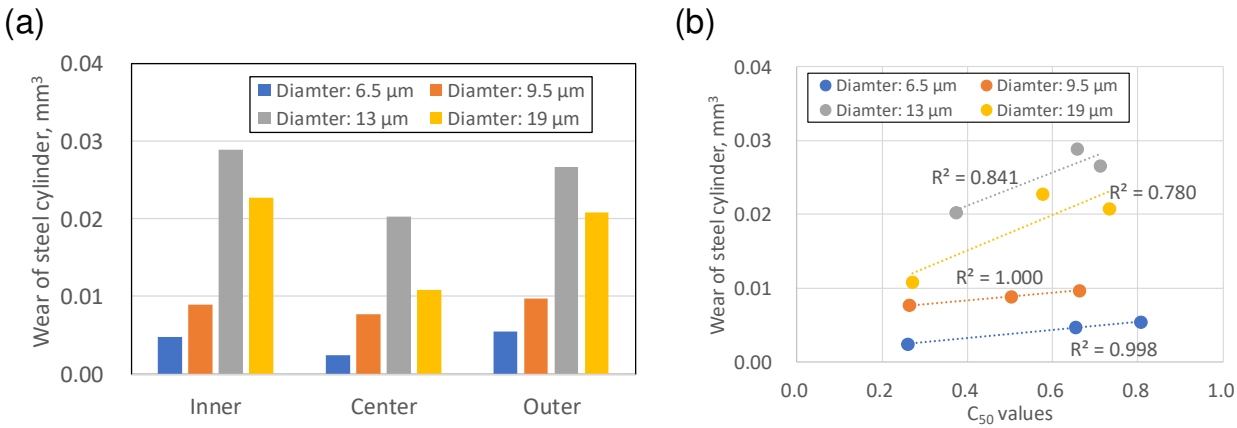

Fig. 37 (a) Wear of the steel cylinders at positions corresponding to the inner, center, and outer positions of the composite ring after 50,000 cycles. (b) Relationship between the C_{50} values on the sliding surface of the composite and the wear of the steel cylinders at each position after 50,000 cycles.

Fig. 38 shows the total GF area and total GF perimeter, which is correlated to the total contact area between the GF and PA66 on the sliding surface, for the composites with different GF diameter values. No difference in the total GF area was observed between the different positions on the composite surface. In contrast, the total GF perimeter decreased with increasing GF diameter. The total GF perimeter of the 6.5 μm diameter GFs was 2.00–2.48 times larger than that of the 19 μm diameter ones. This result can explain the difference in the wear of the steel counterpart by composites with different GF diameters. The interfacial shear strength between PA66 and the GFs was the same regardless of the GF diameter because the same PA66 and GF surface treatment agent was used for all the samples [31]. Therefore, the total energy of the adhesion between the PA66 and GFs increased with increasing total GF perimeter (i.e., the contact area between the PA66 and GFs). With greater

adhesion energy, more sliding cycles are required to induce interfacial peeling between the GFs and PA66, and the exposure of the GF edges due to the shear energy of sliding is reduced. Furthermore, the fracture strength of individual small-diameter GFs is lower than that of large-diameter fibers; thus, small GFs on the sliding surface of the composite are more easily damaged by the shear stress of sliding. GF debris was present in the grease at the end of test; however, this debris had little aggressive effect on the steel due to the two-body abrasion mode of the steel counterpart. In contrast, the larger GFs were less easily damaged or removed by the shear stress of sliding. Therefore, the effect of the two-body abrasion was more severe. Based on these two phenomena, we concluded that the steel wear can be reduced by decreasing the GF diameter.

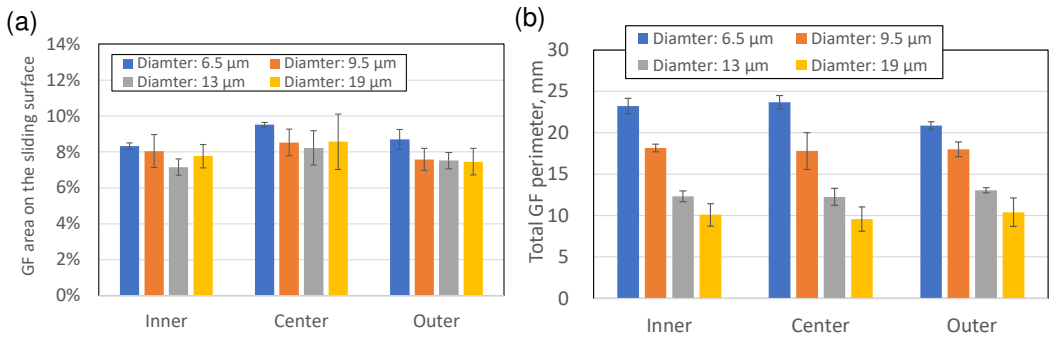

Fig. 38 (a) Total GF area and (b) total GF perimeter on the sliding surfaces of composites that differed only in GF diameter. Three measurements were conducted at each position.

The wear debris from the steel counterpart was also analyzed. As shown in Fig. 39, the sliding surfaces of the composites with GF diameters of 6.5 μm and 19 μm were observed using SEM after 50,000 cycles. Energy-dispersive X-ray spectroscopy (EDX) analysis was conducted to observe the distribution of the attached Fe, which is related to the wear debris of the steel counterpart. Afterwards, binarization of Fe particles in the image and particle analysis were conducted using the software package image J. Only particles with surface areas of 5 μm^2 or more were considered due of the noisiness of EDX images. Fig. 40 shows the relationship between the size of the Fe particles and the cumulative frequency of the Fe particle area. The average size of the Fe wear debris for the composite with a GF diameter of 19 μm was much larger than that of the composite with 6.5 μm fibers. The area of the Fe wear debris at 50% cumulative frequency of Fe particle area for the 19 μm diameter composite was 34.2 μm^2; this value was 3.45 times higher than that of the 6.5 μm diameter composite (9.9 μm^2). This was attributed to the size of the GFs on the sliding surface of the composite, which had a significant effect on the two-body abrasion of the steel.

Diameter of GF	Original image	EDX image of Fe ⇒Binarization	Particle analysis (only > 5 μm² particles)
6.5 μm	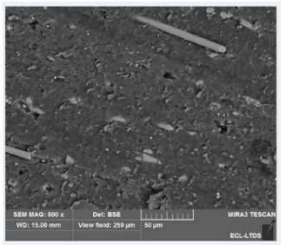	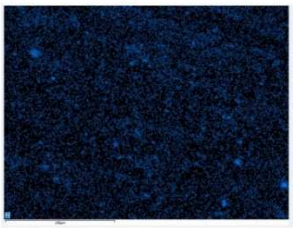	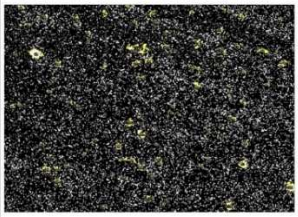
19 μm	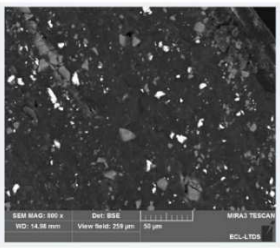	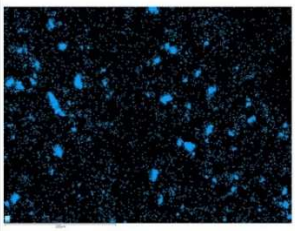	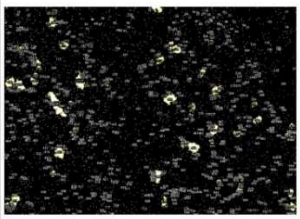

Fig. 39 SEM observation of the sliding surfaces of composites with different GF diameters after a 50,000 cycle sliding test and image analysis of the Fe wear debris.

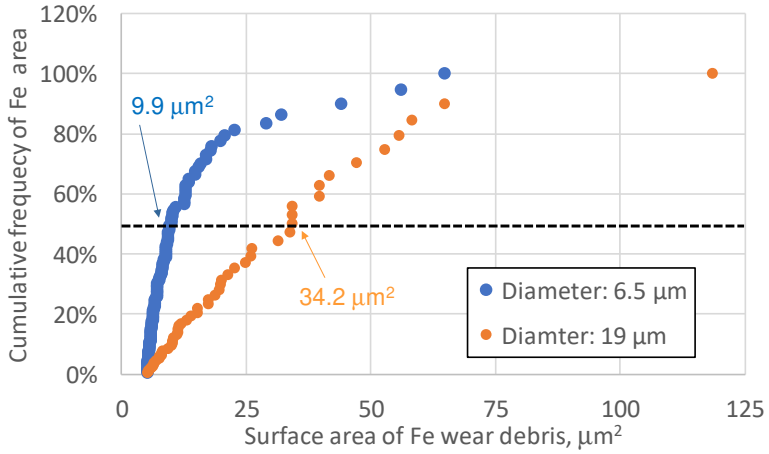

Fig. 40 Relationship between the surface area of the Fe wear debris and the cumulative frequency of Fe area.

Fig. 41 schematically illustrates the effect of the GF diameter on the tribological properties of the GF-reinforced PA66 composite and steel system discussed above.

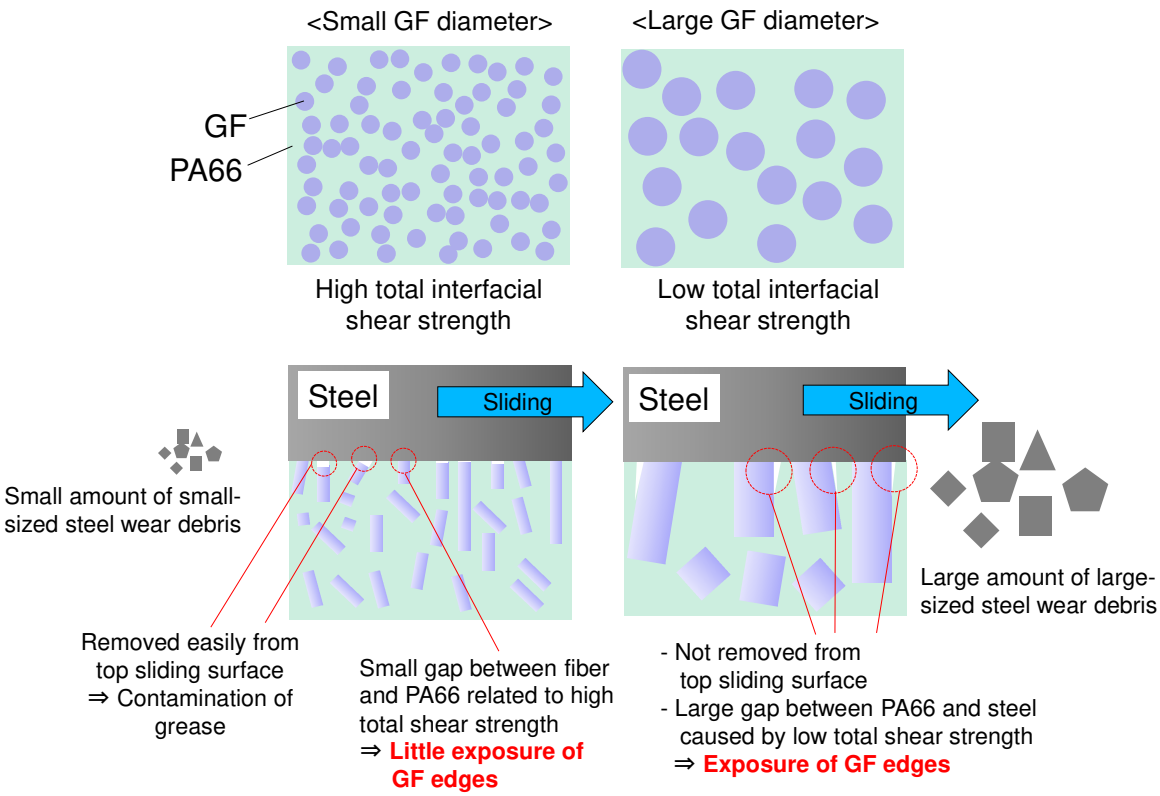

Fig. 41 Schematic of the effects of the GF diameter on the tribological properties.

4. Conclusions

The tribological properties of GF-reinforced PA66 composites in contact with carbon steel were studied under grease-lubricated conditions. The effects of the composition of the composite on the tribological properties were investigated with the aim of developing a composite with optimized tribological properties. The main findings have been highlighted below.

1) Effects of the interfacial shear strength between PA66 and GF

High interfacial shear strength between the PA66 matrix and the GFs reduced the friction coefficient and wear of the composite. Good adhesion between PA66 and GF prevented the degradation of the mechanical properties of the composite surface during sliding, which is related to the peeling of glass fibers and the initiation and propagation of the scratches. The wear resistance of the steel counterpart was also enhanced by increasing the interfacial shear strength, as high interfacial strength prevents the exposure of GF edges, which have a strongly aggressive effect on the steel counterpart. The difference in the interfacial shear strength resulting from the use of different glass fiber surface treatment agents was discussed quantitatively using a modified Kelly–Tyson model that accounts for the length and orientation of the fibers.

2) Effects of the molecular mass of PA66

The wear resistances of both the GF-reinforced PA66 composite and the steel counterpart were improved by

increasing the molecular mass of the PA66. The high elongation of the high-molecular-mass PA66 reduced the interfacial peeling between GF and PA66 due to the shear stress induced by sliding and prevented the exposure of the GF edges, which have a strongly aggressive effect on the steel counterpart via a two-body abrasive wear mode. Additionally, the high toughness of the high-molecular-mass PA66 reduced the propagation of scratches on PA66, which originated at the interface between PA66 and the GFs, and enhanced the wear and creep resistance of the composite.

3) Effects of GF diameter

The wear of the steel counterparts reduced with decreasing GF diameter. Image analysis revealed that the total interfacial area between GF and PA66 increased when small-diameter GFs were used. This indicates that surfaces with high interfacial adhesion energy can bear higher sliding energies without interfacial peeling between GF and PA66. The wear and creep resistances of the composite also improved when smaller-diameter GFs were used because the strength and toughness of the composite were enhanced by the increase in the interfacial adhesion area.

References

[1] S.M. Lee, M.W. Shin, H. Jangn, Effect of carbon-nanotube length on friction and wear of polyamide 6,6 nanocomposites, Wear 320 (2014) 103-110. https://doi.org/10.1016/j.wear.2014.08.011

[2] M.T. Lates, R. Velicu, C.C. Gavrila, Temperature, pressure, and velocity influence on the tribological properties of PA66 and PA46 Polyamides, Materials 12 (20) (2019) 3452. https://doi.org/10.33a90/ma12203452

[3] D.W. Gebretsadik, J. Hardell, B.Prakash, Friction and wear characteristics of PA 66 polymer composite/316L stainless steel tribopair in aqueous solution with different salt levels, Tribol. Int.141 (2020) 105917. https://doi.org/10.1016/j.triboint.2019.105917

[4] J. Chen, H. Xu, C. Liu, L. Mi, C. Shen, The effect of double grafted interface layer on the properties of carbon fiber reinforced polyamide 66 composites. Composites Sci. and Technol. 168 (2018) 20-27. https://doi.org/10.1016/j.compscitech.2018.09.007

[5] B. Sarita, S. Senthilvelan, Effects of lubricant on the surface durability of an injection molded polyamide 66 spur gear paired with a steel gear, Tribol. Int. 137 (2019) 193–211. https://doi.org/10.1016/j.triboint.2019.02.050

[6] S. Senthilvelan, R. Gnanamoorthy, Fiber reinforcement in injection molded nylon 6/6 spur gears, Appl. Compos. Mater. 13 (2006) 237–248. https://doi.org/10.1007/s10443-006-9016-9

[7] J. Tavčar, G. Grkman, J. Duhovnik, Accelerated lifetime testing of reinforced polymer gears, J. of Advanced Mec. Des., Sys., and Man. 12 (2018) 1-13. https://doi.org/10.1299/jamdsm.2018jamdsm0006

[8] Y. Zhang, C. Purssell, K. Mao, S. Leigh, A physical investigation of wear and thermal characteristics of 3D printed nylon spur gears. Tribol. Int., 141 (2020) 105953. https://doi.org/10.1016/j.triboint.2019.105953

[9] H. Oh, M.H. Azarian, C. Morillo, M. Pecht, E. Rhem, Failure mechanisms of ball bearings under lightly loaded, non-accelerated usage conditions, Tribol. Int. 81 (2015) 291–299. https://doi.org/10.1016/j.triboint.2014.09.014

[10] J. Kohout, Strength changes of moulded polyamide composite caused by thermal oxidation, J. of Mat. Sci. 34 (1999) 843-849. https://doi.org/10.1023/A:1004593417901

[11] M. Harrass, K. Friedrich, A.A. Almajid, Tribological behavior of selected engineering polymers under rolling contact. Tribol. Int. 43 (2010) 635–646. https://doi.org/10.1016/j.triboint.2009.10.003

[12] T. Kunishima, K. Miyake, T. Kurokawa, H. Arai, Clarification of tribological behavior on tooth surface of resin worm gear for electric power steering, JTEKT Eng. J. English Edition, 1013E (2016) 27–33.

[13] G.H. Kim, J.W. Lee, T.Il. Seo, Durability characteristics analysis of plastic worm wheel with glass fiber reinforced polyamide, Materials 6 (2013) 1873–1890. https://doi.org/10.3390/ma6051873

[14] A. Bormuth, J. Zuleeg, C. Schmitz, R. Schmitz, M. Pfadt and H. Meven, Lubrication of plastic worm gears, Power Transmission Eng. Aug. (2019) 42-47.

[15] Y.K. Chen, O.P. Modi, A.S. Mhay, A. Chrysanthou, J.M. O'Sullivan, The effect of different metallic counterface materials and different surface treatments on the wear and friction of polyamide 66 and its composite in rolling-sliding contact, Wear 255 (2003) 714–721. https://doi.org/10.1016/S0043-1648(03)00054-1

[16] S. S. Kim, M. W. Shin, H. Jang, Tribological properties of short glass fiber reinforced polyamide 12 sliding on medium carbon steel, Wear 274-275 (2012) 34-42. https://doi.org/10.1016/j.wear.2011.08.009

[17] S.N. Kukureka, C.J. Hooke, M. Rao, P. Liao, Y. K. Chen, Effect of fibre reinforcement on the friction and wear of polyamide 66 under dry rolling-sliding contact, Tribol. Int. 32 (1999) 107–116. https://doi.org/10.1016/S0301-679X(99)00017-1

[18] J.W. Kim, H. Jangn, Jin Woo Kim, Friction and wear of monolithic and glass-fiber reinforced PA66 in humid conditions, Wear 309 (2014) 82-88. https://doi.org/10.1016/j.triboint.2019.105917

[19] T. Kunishima, Y. Nagai, T, Kurokawa, G. Bouvard, J-C. Abry, V. Fridrici, P. Kapsa, Tribological behavior of glass fiber reinforced-PA66 in contact with carbon steel under high contact pressure, sliding and grease lubricated conditions, Wear (2020). https://doi.org/10.1016/j.wear.2020.203383

[20] T. Kunishima, S. Nagai, T. Kurokawa, J. Galipaud, G. Guillonneau, G. Bouvard, J.-Ch. Abry, C. Minfray, V. Fridrici, Ph. Kapsa, Effects of temperature and addition of zinc carboxylate to grease on the tribological properties of PA66 in contact with carbon steel, Tribology Int. (2020) 106578. https://doi.org/10.1016/j.triboint.2020.106578

[21] S. Yu, KH. Oh, JY. Hwang, S.H. Hong, The effect of amino-silane coupling agents having different molecular structures on the mechanical properties of basalt fiber-reinforced polyamide 6,6 composites, Compos. Part B 163 (2019) 511-521. https://doi.org/10.1016/j.compositesb.2018.12.148

[22] D. Frihi, A. Layachi, S. Gherib, G. Stoclet, K.M-Varlot, H. Satha, R. Seguela, Crystallization of glass-fiber-reinforced polyamide 66 composites: Influence of glass-fiber content and cooling rate, Compos. Sci. Tec. 130 (2016) 70-77. https://doi.org/10.1016/j.compscitech.2016.05.007

[23] M. Liao, Y. Yang, H. Hamada, Mechanical performance of glass woven fabric composite: Effect of different surface treatment agents, Compos. Part B 86 (2016) 17-26. https://doi.org/10.1016/j.compositesb.2015.08.084

[24] D. Zhao, H. Hamada, Y. Yang, Influence of polyurethane dispersion as surface treatment on mechanical, thermal and dynamic mechanical properties of laminated woven carbon-fiber-reinforced polyamide 6

composites, Compos. Part B: Engineering 160 (2019) 535-545. https://doi.org/10.1016/j.compositesb.2018.12.105

[25] N.G. Karsli, T. Yilmaz, O. Gul, Effects of coupling agent addition on the adhesive wear, frictional and thermal properties of glass fiber-reinforced polyamide 6,6 composites, Polym. Bull. 75 (2018) 4429-4444. https://doi.org/10.1007/s00289-018-2278-1

[26] N.G. Karsli, S. Demirkol, T. Yilmaz, Thermal aging and reinforcement type effects on the tribological, thermal, thermomechanical, physical and morphological properties of poly (ether ether ketone) composites, Compos. Part B 88 (2016) 253-263. https://doi.org/10.1016/j.compositesb.2015.11.013

[27] M. Sharma, J. Bijwe, Influence of fiber–matrix adhesion and operating parameters on sliding wear performance of carbon fabric polyethersulphone composites, Wear 271 (2011) 2919-2927. https://doi.org/10.1016/j.wear.2011.06.012

[28] M. Sharma, J. Bijwe, P. Mitschang, Wear performance of PEEK–carbon fabric composites with strengthened fiber–matrix interface, Wear 271 (2011) 2261-2268. https://doi.org/10.1016/j.wear.2010.11.055

[29] M.W. Shin, S.S. Kim, H. Jang, Friction and wear of polyamide 66 with different weight average molar mass, Tribol. Lett. 44 (2011) 151–158. https://doi.org/10.1007/s11249-011-9833-3

[30] T. Kunishima, T. Kurokawa, H. Arai, V. Fridrici, P. Kapsa, Reactive extrusion mechanism, mechanical and tribological behavior of fiber reinforced polyamide 66 with added carbodiimide, Mater. Des. 188 (2020) 108447.
https://doi.org/10.1016/j.matdes.2019.108447

[31] M. Kurokawa, Y. Uchiyama, T. Iwai, S. Nagai, Performance of plastic gear made of carbon fiber reinforced polyamide 12, Wear 254 (2003) 468–473. https://doi.org/10.1016/S0043-1648(03)00020-6

[32] F. Ramsteiner, R. Theysohn, The influence of fibre diameter on the tensile behaviour of short-glass-fibre reinforced polymers, Compsi. Sci. Tec., 24 3 (1985) 231-240.

[33] K. Ozawa, T.S. Kim, D. Tsunoda, Y. Arao, N. Taniguchi, T. Nisshiwaki, A. Hosoi, H. Kawada, Influence of fiber diameter on impact tensile properties of injection-molded long glass fiber reinforced polyamide, Trasaction of the JSME, 82 839 (2016) 1-17. https://doi.org/10.1299/transjsme.15-00657

[34] T. Murakami, T. Takajo, Research work for the improvement of the durability of glass fiber-reinforced nylon 66 by modifying the glass fiber diameter, SAE Technical Paper 32 (2006). https://doi.org/10.4271/2006-32-0032

[35] X. Chen, R. Jiao, K.S. Kim, On the Ohno–Wang kinematic hardening rules for multiaxial ratcheting modeling of medium carbon steel, Int. J. Plasticity, 21 (2005) 161-184. https://doi.org/10.1016/j.ijplas.2004.05.005

[36] S.K. Paul, Prediction of non-proportional cyclic hardening and multiaxial fatigue life for FCC and BCC metals under constant amplitude of strain cycling, Mat. Sci. and Eng.: A, 656 (2016) 111-119. https://doi.org/10.1016/j.msea.2016.01.029

[37] M. Okane, T. Shitaka, M. Ishida, T. Chaki, T. Yasui, M. Fukumoto, Fatigue Properties of Butt Welded Aluminum Alloy and Carbon Steel Joints by Friction Stirring, J. Phys.: Conf. Ser. 843 (2017) https://doi.org/10.1088/1742-6596/843/1/012040

[38] Y. Yamamoto, M. Hashimoto, Friction and wear of water lubricated PEEK and PPS sliding contacts: Part 2. Composites with carbon or glass fibre, Wear 257 (2004) 181-189. https://doi.org/10.1016/j.wear.2003.12.004

[39] D-X. Li, X. Deng, J. Wang, J. Yang, X. Li, Mechanical and tribological properties of polyamide 6–polyurethane block copolymer reinforced with short glass fibers, Wear 269 (2010) 262-268. https://doi.org/10.1016/j.wear.2010.04.004

[40] D.M.Laura, H.Keskkula, J.W.Barlow, D.R.Paul, Effect of glass fiber surface chemistry on the mechanical properties of glass fiber reinforced, rubber-toughened nylon 6, Polymer 43 (2002) 4673-4687 https://doi.org/10.1016/S0032-3861(02)00302-6

[41] A. Kelly, W.R. Tyson, Tensile properties of fiber-reinforced materials: Copper/tungsten and copper/molybdenum, J. Mechanics Phys. Solids 13 (1965) 329–350. https://doi.org/10.1016/0022-5096(65)90035-9

[42] H. Fukuda, T. Chou, A probability theory of the strength of short-fibre composites with variable fibre length and orientation, J. Mat. Sci. 17 (1982) 1003-1011. https://doi.org/10.1007/BF00543519

[43] R. Wongpajan, S. Mathurosemontri, R. Takematsu, H.Y. Xu, P. Uawongsuwan, S. Thumsorn, H. Hamada, Interfacial shear strength of glass fiber reinforced polymer composites by the modified rule of mixture and Kelly-Tyson model, Energy Procedia 89 (2016) 328-334. https://doi.org/10.1016/j.egypro.2016.05.043

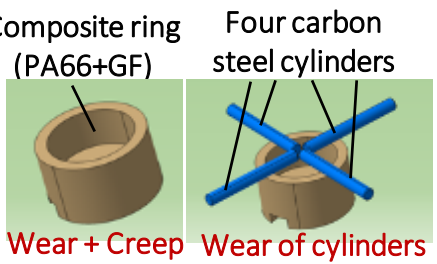

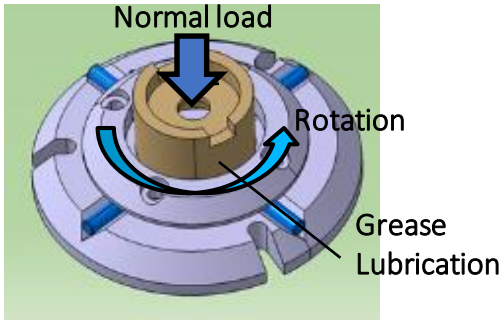

Parameter in this work

1) Interfacial adhesion between PA66 and GF
2) Molecular mass (Mw) of PA66
3) GF diameter

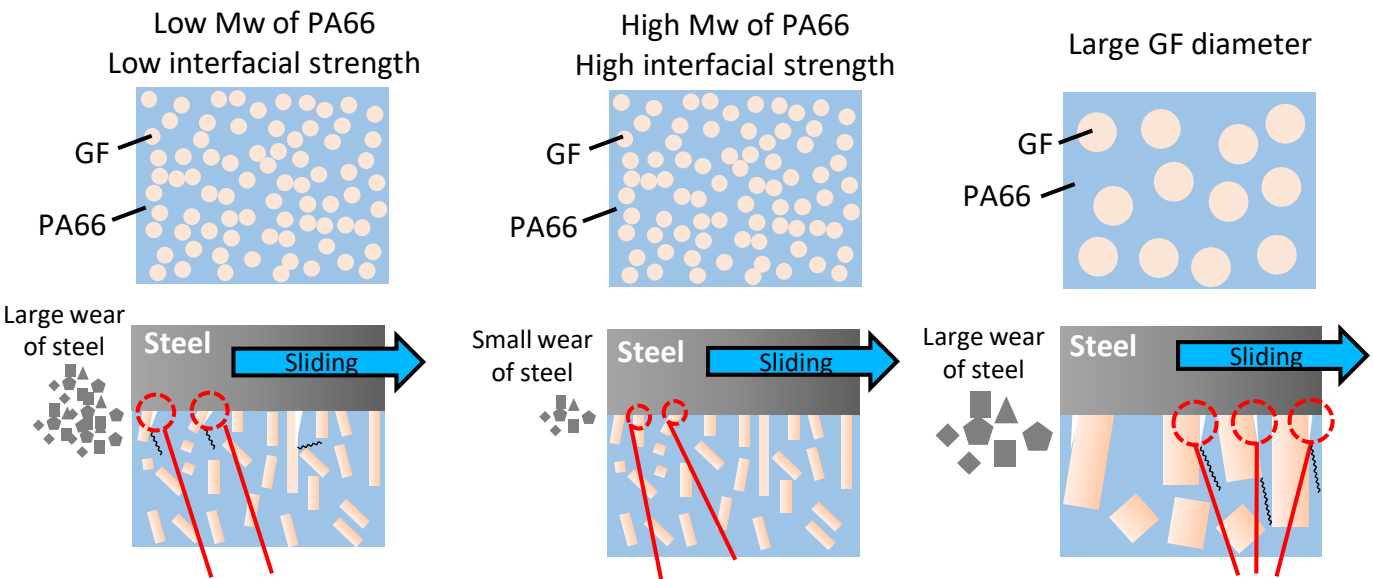

Large gap caused by low shear strength and toughness of PA66
⇒ Exposure of GF edges
Propagation of PA66 scratches
Worse composite wear resistance

Small gap caused by high shear strength and toughness of PA66
⇒ Little exposure of GF edges
Good composite wear resistance

Large gap caused by low total shear strength
⇒ Exposure of GF edges and propagation of PA66 scratches